

VLT/MAGELLAN SPECTROSCOPY OF 29 STRONG LENSING SELECTED GALAXY CLUSTERS

MAURICIO CARRASCO^{1,2}, L. FELIPE BARRIENTOS^{2,3}, TIMO ANGUITA^{4,3}, CRISTINA GARCÍA-VERGARA^{2,5}, MATTHEW BAYLISS^{6,7}, MICHAEL GLADDERS⁸, DAVID GILBANK⁹, H.K.C. YEE¹⁰, AND MICHAEL WEST¹¹

Submitted to the Astrophysical Journal, November 4, 2016

ABSTRACT

We present an extensive spectroscopic follow-up campaign of 29 strong lensing (SL) selected galaxy clusters discovered primarily in the Second Red-Sequence Cluster Survey (RCS-2). Our spectroscopic analysis yields redshifts for 52 gravitational arcs present in the core of our galaxy clusters, which correspond to 35 distinct background sources that are clearly distorted by the gravitational potential of these clusters. These lensed galaxies span a wide redshift range of $0.8 \leq z \leq 2.9$, with a median redshift of $z_s = 1.8 \pm 0.1$. We also measure reliable redshifts for 1004 cluster members, allowing us to obtain robust velocity dispersion measurements for 23 of these clusters, which we then use to determine their dynamical masses by using a simulation-based $\sigma_{DM} - M_{200}$ scaling relation. The redshift and mass ranges covered by our SL sample are $0.22 \leq z \leq 1.01$ and $5 \times 10^{13} \leq M_{200}/h_{70}^{-1} M_{\odot} \leq 1.9 \times 10^{15}$, respectively. We analyze and quantify some possible effects that might bias our mass estimates, such as the presence of substructure, the region where cluster members are selected for spectroscopic follow-up, the final number of confirmed members, and line-of-sight effects. We find that 10 clusters of our sample with $N_{\text{mem}} \gtrsim 20$ show signs of dynamical substructure. However, the velocity data of only one system is inconsistent with a uni-modal distribution. We therefore assume that the substructures are only marginal and not of comparable size to the clusters themselves. Consequently, our velocity dispersion and mass estimates can be used as *priors* for SL mass reconstruction studies and also represent an important step toward a better understanding of the properties of the SL galaxy cluster population.

Subject headings: cosmology: dark matter — gravitational lensing: strong — galaxies: clusters: general — galaxies: kinematics and dynamics — galaxies: evolution

1. INTRODUCTION

Galaxy clusters have long been considered one of the most important cosmological probes due to their privileged position in the hierarchical formation scenario as the most massive and virialized objects. As such, galaxy clusters can inform important tests of the standard concordance cosmological model, and provide unique laboratories for the understanding of dark matter (DM) properties (see Voit 2005, for a review). For example, the number density of galaxy clusters is sensitive to the amplitude of the primordial density fluctuations, and can

therefore be used as a powerful tool for estimating cosmological parameters, so long as the masses and redshifts of clusters are measured with good precision (Evrard et al. 2002; Vikhlinin et al. 2009; Rozo et al. 2010).

In recent years extensive efforts have been made to determine the mass and redshift distribution of samples of galaxy clusters (Böhringer et al. 2004; Gladders & Yee 2005; Burenin et al. 2007; Bleem et al. 2015; Gilbank et al. 2011). Most of these mass measurements are based on baryonic signatures — e.g. optical light, X-ray emission, and the Sunyaev Zel’dovich effect (SZE). However, there are pernicious systematic uncertainties that affect these baryonic signatures, which trace only a small fraction of the total matter content of galaxy clusters. The most robust and direct way to map the total (baryonic and dark) matter distribution in galaxy clusters is through the analysis of gravitational lensing effects, whereby background galaxy profiles are modified by the gravitational potential of foreground clusters, producing shape distortions and apparent flux magnification (see reviews by Bartelmann 2010; Kneib & Natarajan 2011).

In the outer regions of galaxy clusters the gravitational potential produces only tiny distortions that do not constrain the cluster profile individually, and therefore it is necessary to perform statistical measurements of the distortions affecting large ensembles of background galaxies. This is the so-called weak lensing (WL) regime, and the application of WL measurements has become a powerful tool in the recent years (van Uitert et al. 2015; Dahle 2006; Hoekstra & Jain 2008; Okabe et al. 2010;

carrasco@uni-heidelberg.de

¹Zentrum für Astronomie, Institut für Theoretische Astrophysik, Philosophenweg 12, 69120 Heidelberg, Germany

²Instituto de Astrofísica, Pontificia Universidad Católica de Chile. Avda Vicuña Mackenna 4860, Santiago, Chile

³Millennium Institute of Astrophysics, Chile

⁴Departamento de Ciencias Físicas, Universidad Andres Bello, Fernandez Concha 700, Las Condes, Santiago, Chile

⁵Max-Planck-Institut für Astronomie, Königstuhl 17, 69117 Heidelberg, Germany

⁶Department of Physics & Astronomy, Colby College, 5800 Mayflower Hill, Waterville, Maine 04901

⁷Department of Physics, Harvard University, 17 Oxford Street, Cambridge, MA 02138, USA

⁸Department of Astronomy and Astrophysics, and the Kavli Institute for Cosmological Physics, University of Chicago, 5640 South Ellis Avenue, Chicago, IL 60637, USA

⁹South African Astronomical Observatory, PO Box 9, 7935 Observatory, South Africa

¹⁰Department of Astronomy and Astrophysics, University of Toronto, 50 St. George Street, Toronto, Ontario, M5S 3H4, Canada

¹¹Maria Mitchell Observatory, 4 Vestal Street, Nantucket, MA 02554, USA

Umetsu et al. 2014; High et al. 2012). In the innermost region of clusters — the strong lensing (SL) regime — the mass density can be high enough to produce dramatic distortions in the form of giant elongated arcs or multiple images of background sources, which can inform high-precision mass reconstruction studies of the cluster core (e.g. Zitrin et al. 2009, 2012b,a; Limousin et al. 2012). Statistical analysis of samples of galaxy clusters that exhibit the hallmarks — giant arcs and multiply-imaged sources — of strong lensing can also be used in tests of the Λ CDM cosmological model. For example, several different studies comparing observations and predictions for the abundance of giant arcs (“giant arc statistics”) find that simulations under-predict the number of giant arcs on the sky by perhaps as much as an order of magnitude (Bartelmann et al. 1998; Gladders et al. 2003; Li et al. 2006).

In addition to their cosmological applications, the large magnification effects that typically act on strongly lensed background galaxies allows the study of high-redshift galaxies which would otherwise be too faint to be observed. However, cases of bright, high-magnification strong lensing remain relatively rare phenomena, occurring in a only small fraction of galaxy clusters (Horesh et al. 2010). It is therefore always valuable to identify and follow-up new samples of strong lensing galaxy clusters. Identifying new strong lensing samples serves to effectively increase the volume of the early universe that is available for observations (e.g. Bradley et al. 2008; Bouwens et al. 2009; Zheng et al. 2009, 2012; Wuyts et al. 2010, 2014; Bayliss et al. 2011b, 2010; Coe et al. 2013).

In this paper we present the results of a spectroscopic follow-up campaign of 29 SL-selected galaxy clusters with 6.5 – 8.2m class telescopes, discovered primarily in the Second Red-Sequence Cluster Survey (RCS-2; Gilbank et al. 2011). The data presented in this work reveal the nature of the giant arc and multiple-image candidates, increasing the number of spectroscopically confirmed lensed galaxies at high-redshift. From these data we also identify redshifts for more than one thousand cluster member galaxies, which are used to estimate dynamical masses of these clusters. The combination of these results will allow us to derive robust reconstructions of the matter distribution in these galaxy clusters.

This paper is organized as follows: In §2 we describe the cluster sample and summarize the spectroscopic follow-up campaign. In §3 we present the redshift results for the lensed galaxies and cluster members, as well as the final redshift and velocity dispersion of the clusters. In §4 we show the dynamical mass results, while in §5 we analyze the possible systematics that might affect our measurements. Lastly, we summarize the main results and present the final conclusions in §6. Throughout the paper we assume a flat Λ CDM cosmology with $\Omega_m = 0.27$, $\Omega_\Lambda = 0.73$, and $H_0 = 70 h_{70} \text{ km s}^{-1} \text{ Mpc}^{-1}$.

2. OBSERVATIONS

2.1. The SL-selected cluster sample

The cluster sample presented here is a subset of a larger sample of more than one hundred SL-selected clusters that have been identified primarily in RCS-2 imaging data. The median seeing of the RCS-2 survey is $\sim 0.7''$,

making it ideal for the detection and classification of giant arcs. Furthermore, the RCS-2 survey was designed to detect galaxy clusters out to $z \sim 1.1$ using the cluster red-sequence technique (Gladders & Yee 2000) in deep wide-field images. We have searched the resulting galaxy cluster catalog for SL systems, where the SL selection criterion is the presence of one or more giant arcs around a galaxy cluster’s core. The SL-selected clusters identified in the RCS-2 comprise a new sample of giant arcs, the Red-Sequence Cluster Survey Giant Arc (RCSGA; Bayliss 2012, Gladders et al. in prep.) catalog. Giant arc candidates are flagged by multiple members of our team performing independent visual inspections of the entire RCS-2 red-sequence catalog of galaxy clusters, and systems that are flagged by most or all inspectors constitute the SL cluster sample, as described in more detail by Bayliss (2012). We supplement the RCS-2 SL-selected cluster sample with a few systems chosen to fill RA gaps that were similarly selected from the Sloan Digital Sky Survey (SDSS; York et al. 2000).

We performed a comprehensive spectroscopic follow-up of 29 SL-selected galaxy clusters primarily from the RCSGA; 12 of these clusters are previously unpublished. The cluster sample is presented in Table 1, where clusters formerly reported in other studies are marked with their corresponding references. We have adopted the naming convention described in Bayliss et al. (2011b) for giant arcs discovered in RCSGA, given by RCSGA – Jhhmss+ddmss (e.g. Wuyts et al. 2010; Bayliss 2012).

2.2. Imaging

Most of the imaging data presented here have been obtained from the RCS-2 survey. They were collected in queue-scheduled mode with MegaCam at the 3.6m Canada-France-Hawaii Telescope (CFHT), between the semesters 2003A and 2007B inclusive. The RCS-2 data consist in single exposures (without dithering) of 4, 8, and 6 minutes, for the g' , r' , and z' bands, yielding $5\text{-}\sigma$ limiting magnitudes of 24.3, 24.4, and 22.8, respectively (Gilbank et al. 2011). We used the r' and z' bands to identify the red-sequence cluster member candidates, which have been used as targets for the spectroscopic follow-up. Color images from all three bands were used to identify strongly lensed arcs. We have also obtained pre-imaging of our clusters in B , R , and I bands, with the Focal Reducer and low dispersion Spectrograph 2 (FORS2; Appenzeller et al. 1998) at the ESO¹² 8.2m Very Large Telescope (VLT), in queue mode. These pre-imaging data have been mainly used to design the spectroscopic masks but they also help in the search of multiple-image systems.

2.3. Spectroscopy and data reduction

2.3.1. FORS2/VLT

The FORS2/VLT observations were carried out between October 2006 and March 2010 using the Multi-object spectroscopy with exchangeable masks (MXU) mode. The MXU mode allows one both to increase the density of the slits and to freely manipulate the width,

¹² ESO: the European Southern Observatory; <http://www.eso.org/>

Table 1
Summary of VLT/Magellan spectroscopic observations

Target	R.A. ^a (J2000)	Dec ^a (J2000)	Total exposure time		Prev. Rep. ^c
			FORS2/VLT	IMACS/Magellan	
			(Hrs / N ^o masks) ^b		
SDSS J0004-0103	00 04 52.001	-01 03 16.58	2.00 / 2	--	Rigby et al. (2014)
RCS2 J0034+0225 ^d	00 34 28.134	+02 25 22.34	4.33 / 2	--	Voges et al. (1999)
RCS2 J0038+0215	00 38 55.898	+02 15 52.35	4.90 / 2	--	--
RCS2 J0047+0508	00 47 50.787	+05 08 20.02	2.00 / 1	1.67 / 2	--
RCS2 J0052+0433	00 52 10.352	+04 33 33.31	1.67 / 1	3.33 / 2	--
RCS2 J0057+0209	00 57 27.869	+02 09 33.98	3.48 / 2	--	--
RCS2 J0252-1459	02 52 41.474	-14 59 30.38	1.33 / 1	0.67 / 1	Horesh et al. (2010)
RCS2 J0309-1437	03 09 44.096	-14 37 34.38	2.15 / 2	1.83 / 1	Bayliss (2012)
RCS2 J0327-1326	03 27 27.174	-13 26 22.90	2.00 / 1	2.00 / 2	Wuyts et al. (2010)
RCS2 J0859-0345	08 59 14.486	-03 45 14.63	3.33 / 2	--	Cabanac et al. (2007)
RCS2 J1055-0459	10 55 35.647	-04 59 41.60	5.17 / 4	1.00 / 1	Wittman et al. (2006)
RCS2 J1101-0602	11 01 54.093	-06 02 32.02	1.00 / 1	--	Anguita et al. (2012)
RCS2 J1108-0456	11 08 16.835	-04 56 37.62	2.00 / 2	1.17 / 1	--
SDSS J1111+1408	11 11 24.483	+14 08 50.82	2.17 / 2	--	Wuyts et al. (2012)
RCS2 J1119-0728	11 19 11.925	-07 28 17.51	2.17 / 2	--	--
RCS2 J1125-0628	11 25 28.940	-06 28 39.04	2.67 / 2	1.33 / 1	--
RCS2 J1250+0244	12 50 41.890	+02 44 26.57	1.67 / 2	1.67 / 1	White et al. (1997)
RCS2 J1511+0630	15 11 44.681	+06 30 31.79	2.67 / 2	--	--
SDSS J1517+1003	15 17 02.587	+10 03 29.27	2.00 / 2	2.33 / 1	Szabo et al. (2011)
SDSS J1519+0840	15 19 31.213	+08 40 01.43	4.00 / 3	1.33 / 1	Hao et al. (2010)
RCS2 J1526+0432	15 26 14.914	+04 32 48.01	2.00 / 2	--	--
SDSS J2111-0114	21 11 19.307	-01 14 23.95	2.17 / 2	2.67 / 1	Bayliss et al. (2011b)
SDSS J2135-0102	21 35 12.040	-01 02 58.27	6.11 / 4	2.00 / 1	Szabo et al. (2011)
RCS2 J2147-0102	21 47 37.172	-01 02 51.93	3.00 / 2	1.50 / 1	--
RCS2 J2151-0138 ^d	21 51 25.950	-01 38 50.14	1.50 / 2	1.00 / 1	Voges et al. (1999)
SDSS J2313-0104	23 13 54.514	-01 04 48.46	1.50 / 2	1.17 / 1	Geach et al. (2011)
RCS2 J2329-1317	23 29 09.528	-13 17 49.26	4.08 / 4	1.33 / 1	--
RCS2 J2329-0120	23 29 47.782	-01 20 46.89	2.00 / 1	2.00 / 1	White et al. (1997)
RCS2 J2336-0608	23 36 20.838	-06 08 35.81	3.00 / 2	--	--

^a Coordinates correspond to the BCG centroids in sexagesimal degrees (J2000).

^b Total integration time for lensed galaxy candidates (for instrument/telescope), distributed across the number of masks listed in the spectroscopic follow-up. Slits targeting to cluster members varied between each mask; therefore, the total integration time shown in this table does not necessarily correspond to the total integration time of these objects.

^c Clusters formerly identified and/or described in previous studies.

^d Clusters reported in the ROSAT all-sky bright source catalog (Voges et al. 1999) as RX J0034.4+0225 and RX J2151.4-0139, respectively.

length, and orientation of the slits, making it ideal for spectroscopy in dense regions like the cluster cores. The masks were strategically positioned in the center of each cluster in order to prioritize giant arcs and lensed galaxy candidates. The central slit widths were set to 1'', while their length was varied depending on the arc candidate size, typically between 12'' to 25''. Subsequently, the masks were filled in with slits placed on red-sequence selected cluster members, prioritizing brighter galaxies ahead of fainter ones. The length of these slits was set between 6'' and 12'', depending on each member candidate size. Two masks were usually constructed for each cluster, although some of them had up to four. In order to increase the flux of our lensed galaxy candidates, we fixed the slits located at the arc positions. On the other hand, with the purpose of increasing the number of spectroscopically confirmed cluster members, we varied the slits located on member candidates between each mask. We used a low spectral resolution instrument setup by combining the GRIS_150I+27 grism and GG435+81 filter, and adopted a 2×2 binning in order to improve the signal-to-noise ratio of the spectra. This configuration results in a final dispersion of 6.9 Å per image pixel, and covers a spectral range of $\Delta\lambda \sim 4300 - 10500$ Å, with our highest sensitivity in the interval $\Delta\lambda \sim 4500 - 9000$

Å, due to the transmission efficiency of the filter used, as well as to the detector's quantum efficiency. Depending on the intrinsic features of each target, we varied the exposure times between 1200 - 3000 seconds. The total integration time for each galaxy cluster is reported in Table 1.

The basic data reduction steps consisted of bias subtraction, flat-fielding, wavelength calibration, and sky subtraction. These steps were carried out by using the ESO Recipe Execution Tool (EsoRex¹³) and the Common Pipeline Library (CPL¹⁴). The wavelength calibration was done by comparison to the standard He+Ne+Ar lamp observations. Due to the nature of giant arcs, long and elongated objects, the sky subtraction was a complicated task and was carried out independently. The other advanced steps consisted of the removal of cosmic rays, the 1D spectra extraction and the average of multiple spectra for each source. These steps were performed using our own IDL routines, inspired by the optimal extraction algorithm by Horne (1986).

2.3.2. IMACS/Magellan

¹³ <http://www.eso.org/sci/software/cpl/esorex.html>

¹⁴ <http://www.eso.org/sci/software/cpl>

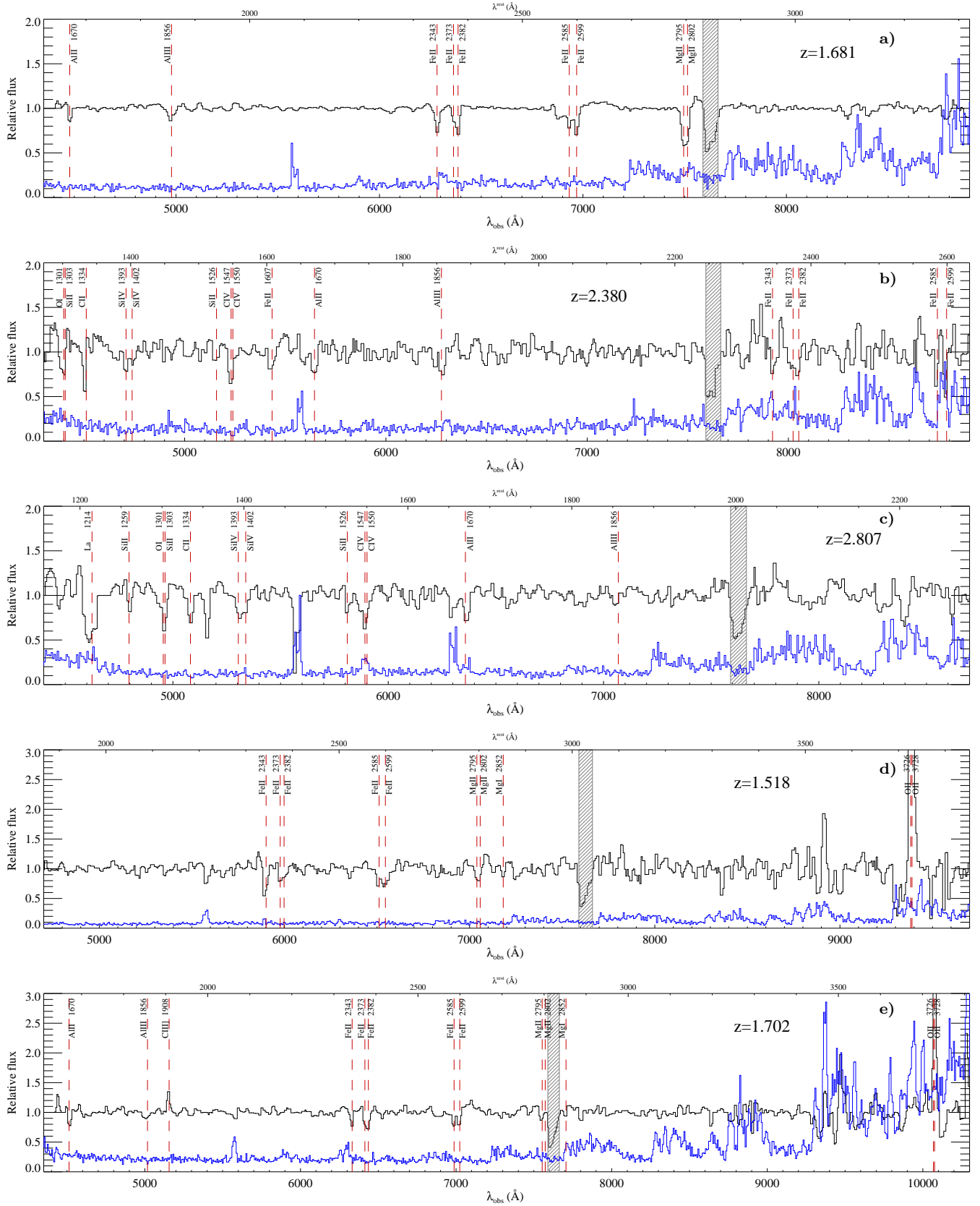


Figure 1. FORS2/VLT spectra for five lensed galaxies with highly reliable redshift measurements, labeled as class 3. Spectra are displayed in the observer-frame and smoothed to match the spectral resolution of the data. The blue histograms correspond to the error array for the spectra, and the locations of spectral lines are identified by red dashed lines and labeled with their corresponding ion name and rest-frame wavelength. The telluric A Band absorption feature is indicated by a vertical shaded region. From top to bottom the spectra in each panel correspond to the following sources in Table 2 – a) SDSS J0004–0103, S1; b) RCS2 J0034+0225, S1; c) RCS2 J1055–0459, S1; d) RCS2 J0309–1437, S1; e) RCS2 J0327+1326 S1.

We have also performed spectroscopic observations with the Inamori Magellan Areal Camera and Spectrograph (IMACS; Dressler et al. 2006, 2011) on the 6.5m Magellan (Baade) telescope at LCO¹⁵. The IMACS/Magellan observations were collected during 6 different runs between June 2008 and March 2011. We used the Gladders Image-Slicing Multislit Option (GISMO¹⁶) at IMACS, which allows high-efficiency spectroscopy for galaxy clusters, obtaining spectra from $\sim 20 - 60$ members in a single spectroscopic mask. The mask design was performed following the same strategy described above, although the slit length was considerably shorter than the VLT data. The GISMO-IMACS masks had slits that were consistently $\sim 5.5'' - 6.5''$ long. The IMACS f/4 camera and the grating of 300 lines/mm were used to obtain 2×2 binning spectra, covering an effective spectral range of $\Delta\lambda \sim 4800 - 8000 \text{ \AA}$, with final dispersion of $\sim 1.5 \text{ \AA}$ per image pixel. The exposure time of the GISMO-IMACS observations varied between 2400 – 9600 seconds. The total integration time for each cluster is reported in Table 1.

The GISMO-IMACS data were reduced using the Carnegie Observatories System for MultiObject Spectroscopy (COSMOS¹⁷) pipeline. The COSMOS reduction process consisted of bias subtraction, flat-fielding and a wavelength calibration using comparison arcs. The wavelength solutions have typical rms $\lesssim 0.5 \text{ \AA}$. The sky subtraction was carried out by constructing a cosmic ray-cleaned median sky spectrum for each slit, which was then subtracted from the slit image. Finally, the 1D spectra extraction and the combination of different exposures were performed using our own IDL routines.

3. RESULTS

3.1. Redshift measurements

The spectroscopic redshifts were determined with two independent methods for Magellan and VLT data. In the first procedure, galaxy redshifts were measured by cross-correlating the spectra with galaxy spectral templates of the SDSS Data Release 7 (DR7; Abazajian et al. 2009) using the RVSAO/XCSAO package for IRAF¹⁸ (Kurtz & Mink 1998). The spectral features in each spectrum were confirmed by visual inspection with the 2D spectra. This technique yielded accurate redshift measurements for high/medium signal-to-noise spectra. However, most of the lensed galaxies have a low signal-to-noise ratio, and thus, the redshift results of these cross-correlations have low reliability. In order to determine reliable spectroscopic redshift for all lensed galaxies, we used a second method; we assigned redshifts to individual spectra by identifying a set of lines at a common redshift, fitting a Gaussian profile to each line in order to determine their central wavelength, and taking the mean redshift of the entire set of lines. The sets of emission and absorption lines used in the redshift measurements of the

lensed galaxies varied significantly among the different source spectra (Bayliss et al. 2011b). Most emission lines observed in the giant arc spectra coincided with CIII] $\lambda 1908.73 \text{ \AA}$, [OII] $\lambda 3727.09, 3729.88 \text{ \AA}$, H β $\lambda 4862.68 \text{ \AA}$, [OIII] $\lambda 4960.30, 5008.24 \text{ \AA}$, which usually correspond to emission lines that come from star forming regions, matching the expectations for high-redshift blue galaxies. Due to the spectral range covered by our instrument setups, these emission lines are observed only in lensed galaxies at $z \lesssim 1.7$. For background sources at higher redshifts, we had to rely on the rest-frame UV features to determine their redshifts. The most common UV metal absorption lines observed in the lensed galaxy spectra were MgII $\lambda 2796.35, 2803.53 \text{ \AA}$, MgI $\lambda 2852.96 \text{ \AA}$, FeII $\lambda 2344.21, 2374.46, 2382.76, 2586.65, 2600.17 \text{ \AA}$, CIV $\lambda 1548.20, 1550.78 \text{ \AA}$, SiII $\lambda 1260.42, 1304.37, 1526.71 \text{ \AA}$, and SiIV $\lambda 1393.76, 1402.77 \text{ \AA}$. For completeness, this second method was also applied to rest of the spectra in our sample. In this case, the redshift measurements of cluster member galaxies were derived from at least three lines; the most used ones correspond to the characteristic lines in older stellar populations (e.g. CaII H&K $\lambda 3934.77, 3969.59 \text{ \AA}$, g-band $\lambda 4305.61 \text{ \AA}$, MgI $\lambda 5168.74, 5174.14, 5185.04 \text{ \AA}$, and NaI $\lambda 5891.61, 5894.13, 5897.57 \text{ \AA}$), although some emission lines were also observed several times (e.g. [OII] $\lambda 3727.09, 3729.88 \text{ \AA}$). The spectral lines used in this analysis were taken from Shapley et al. (2003), Erb et al. (2012), and also from the SDSS spectral line tables¹⁹. It should be noted that all vacuum wavelengths were converted to air wavelengths by applying the IAU standard conversion (Morton 1991), in order to measure redshifts in the air frame.

Redshift errors are mainly due to the combination of the uncertainty in our wavelength calibrations and the statistical uncertainty in the identification of line centers. The median RMS in the wavelength calibration is $\sim 1.4 \text{ \AA}$, which at a central wavelength of $\sim 7000 \text{ \AA}$, results in redshift errors of $\sim \pm 0.0002$. The redshift errors for the high signal-to-noise spectra are distributed around $\sim \pm 0.0005$. These errors are in agreement with the expected ones, since we have to add the uncertainties in the line center identifications. However, the errors increase for low signal-to-noise spectra, assuming values of the order of $\sim \pm 0.001$.

Following the work done by Bayliss et al. (2011b), we classified our redshift measurements into four classes, which describe the confidence level of the redshift measurements. Class 3 redshifts are the highest confidence measurements, typically obtained from more than 4 absorption and/or emission features. These redshift measurements are secure. Given to the high signal-to-noise ratio of the cluster member spectra, virtually all their redshift measurements fall into this category. Approximately 55% of the redshift estimates of the lensed galaxies are also classified as class 3 spectra. Five examples of class 3 lensed galaxy spectra are shown in Figure 1. Class 2 redshifts are medium-confidence measurements. These estimates are based on at least two prominent lines and/or a larger number of low-significance features. The redshifts with this classification are very likely to

¹⁵ LCO: Las Campanas Observatory; <http://www.lco.cl/>

¹⁶ <http://www.lco.cl/telescopes-information/magellan/instruments/imacs/gismo>

¹⁷ <http://code.obs.carnegiescience.edu/cosmos>

¹⁸ IRAF is distributed by the National Optical Astronomy Observatories, which are operated by the Association of Universities for Research in Astronomy, Inc., under cooperative agreement with the National Science Foundation.

¹⁹ <http://www.sdss2.org/dr2/algorithms/linestable.html>

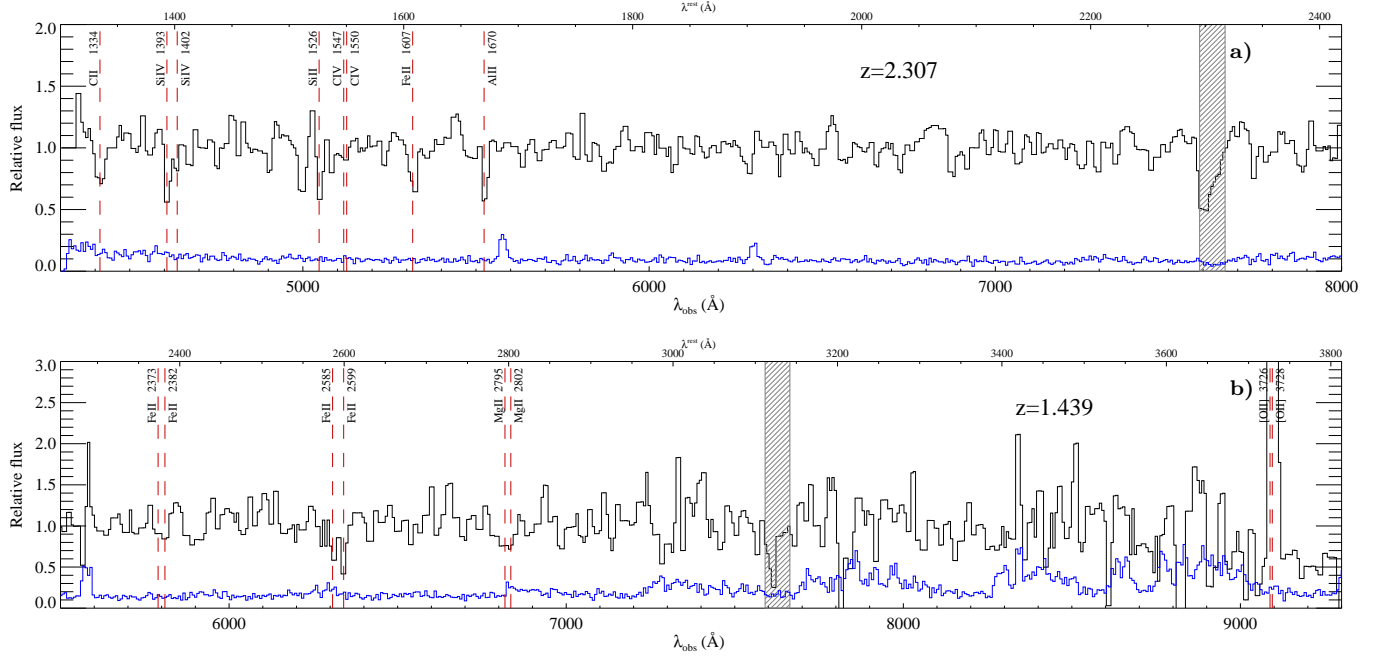


Figure 2. FORS2/VLT spectra for two sources with medium confidence level, labeled as class 2. The spectra are shown in the same manner as in Figure 1. From top to bottom the spectra in each panel correspond to the following sources in Table 2 – a) RCS2 J1250+0244, S1; b) RCS2 J2329–1317, S1.

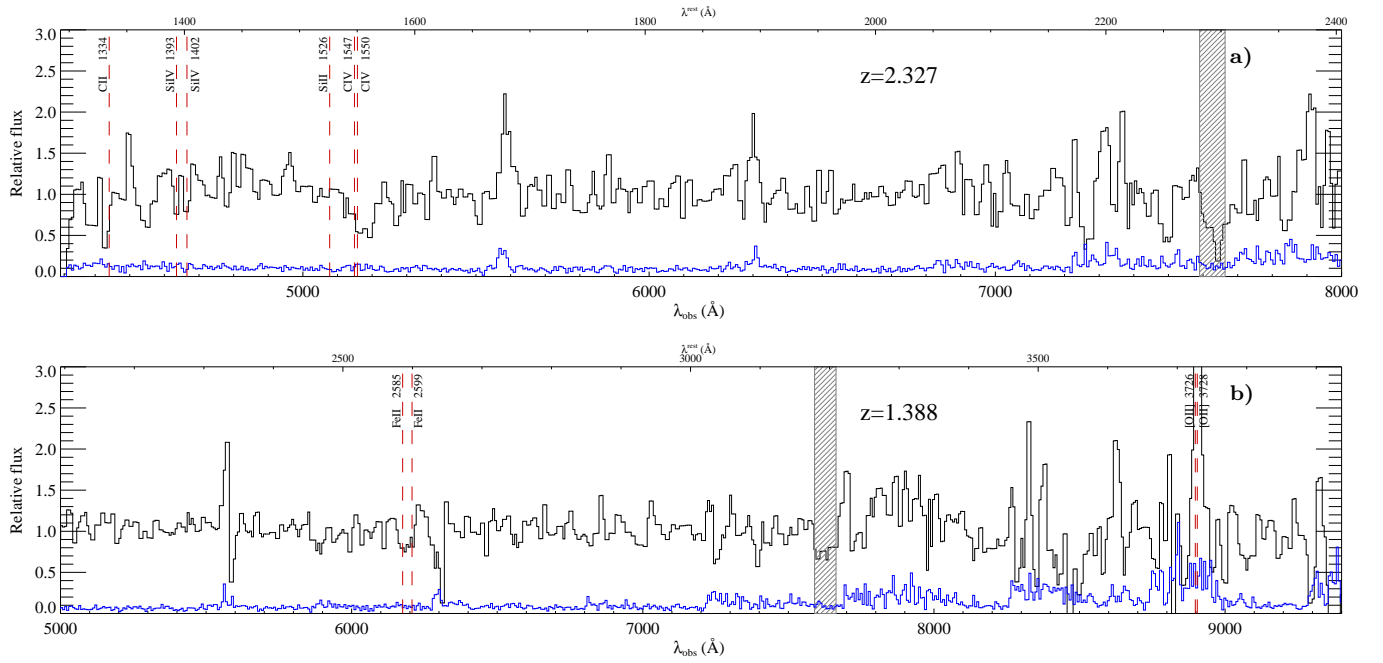


Figure 3. FORS2/VLT spectra for two sources with low confidence level, labeled as class 1. The spectra are displayed in the same fashion as in Figure 1. From top to bottom the spectra in each panel correspond to the following sources in Table 2 – a) RCS2 J2147+0102, S1; b) RCS2 J1108–0456, S1. The spectrum in the top panel is mainly identified at $z = 2.327$ by two weak UV metal absorption lines: SiIV $\lambda 1393.76\text{\AA}$ and SiIV $\lambda 1402.77\text{\AA}$. The spectrum in the bottom panel is identified at $z = 1.388$ by assuming the lone robust emission line feature corresponds to [OII] $\lambda 3727.09, 3729.88\text{\AA}$. There are also two weak UV metal absorption lines matching at this redshift: FeII $\lambda 2586.65\text{\AA}$ and FeII $\lambda 2600.17\text{\AA}$.

be the real redshifts of the corresponding spectra, but there is a small chance that some of them could have been misidentified. Of the order of 21% of the lensed

galaxy spectra fall into this classification. Two examples of class 2 lensed galaxy spectra are shown in Figure 2. Class 1 redshifts are low-confidence measurements,

which are based on few low-significance spectral features and represent the “best-guess” redshift using the available spectral data. Figure 3 shows two examples of class 1 lensed galaxy spectra. Redshift estimates falling in this category correspond to $< 23\%$ of all lensed galaxy spectra. Finally, we have the class 0 redshift for those cases where the spectral analysis shows no evidence of spectral features. There is only one lensed galaxy spectrum in our sample where the redshift measurement completely failed.

3.2. Lensed galaxies

Our spectroscopic analysis has revealed the nature of 52 gravitational arcs present in the core of our galaxy clusters, which correspond to 35 background sources at high-redshift that are clearly distorted by the gravitational potential of these clusters. These lensed galaxies are distributed in a wide redshift range from $0.8 \leq z \leq 2.9$, with a median redshift of $z_s = 1.8 \pm 0.1$, which is consistent with the spectroscopic and color analysis of high-redshift lensed galaxies performed by Bayliss et al. (2011a) and Bayliss (2012) for hundreds of giant arcs identified in the RCS-2 and SDSS surveys. It should be noted that $> 75\%$ of the spectra have a confidence level in their redshift measurements ≥ 2 . The redshift distribution of our lensed galaxy sample and the median redshift found by these previous works are shown in Figure 4. The redshift measurements of all confirmed lensed galaxies are reported in Table 2, with labels that correspond to the label markers in Figures 11 – 18, in Appendix B.

Furthermore, this dataset extends the number of galaxy clusters with spectroscopic confirmation of their SL features available to perform lensing reconstructions of their mass distribution, especially at $z \gtrsim 0.2$.

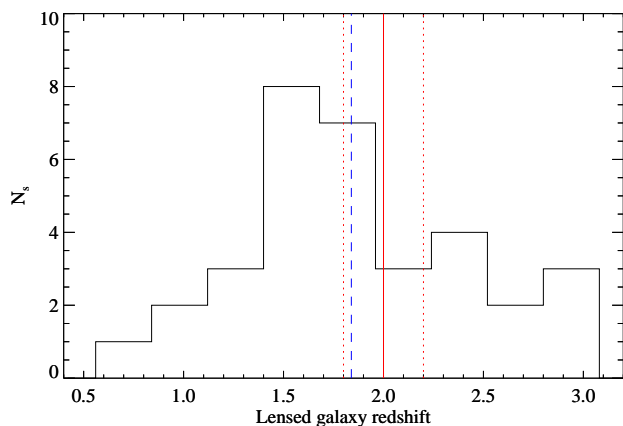


Figure 4. The redshift distribution of the lensed galaxy sample presented in this work. The blue dashed line corresponds to the median redshift of our sample, $z_s = 1.8 \pm 0.1$, while the red solid line correspond to the median redshift found by the spectroscopic and color analysis of high-redshift lensed galaxies - primarily the larger full RCSGA sample - by Bayliss (2012).

3.3. Cluster redshifts and velocity dispersions

The correct determination of cluster members is crucial to avoid biases in the velocity dispersion and mass

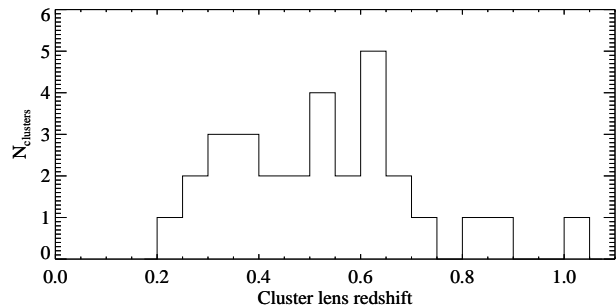


Figure 5. The redshift distribution of our cluster sample, which spans a wide redshift range $0.22 \leq z \leq 1.01$.

measurements (Beers et al. 1990; Ruel et al. 2014). Our selection method of cluster members is an iterative process that starts by applying a cut in the (rest-frame) velocity space of 4000 km s^{-1} , centered at the median redshift of all candidates. Then, the 3σ clipping method is applied to remove the interlopers and the median redshift is recomputed. This process is iterated until the number of members is stable, which usually occurs after the second or third iteration. We have checked possible systematic effects of this procedure by applying the shifting gapper method (Fadda et al. 1996) to those clusters with a large number of galaxies falling into the $\pm 4000 \text{ km s}^{-1}$. The results in both methods are fully consistent.

From this analysis, we have recovered a total of 1004 spectroscopically confirmed cluster, that results in an average of $\langle N_{\text{mem}} \rangle \sim 35$ member galaxies per cluster. The spectroscopic redshift information of all cluster members reported in this work is available as supplementary material in the machine-readable format at the Astrophysical Journal. A portion is shown in Table 3 for guidance regarding its form and content. These data have been used to compute robust measurements of redshift and velocity dispersion of our SL-selected galaxy clusters by applying the bi-weight estimator for robust statistics (Beers et al. 1990). The errors on redshift and velocity dispersion of each cluster were estimated through many bootstrapped realizations, identifying the upper and lower 68% confidence intervals. It should be noted that the errors of individual galaxy redshifts were not considered in the velocity dispersion estimates, because the bias introduced by this exclusion is $< 0.1\%$ for massive clusters (Danese et al. 1980) as in our sample.

The redshift distribution of our cluster sample (Figure 5) spans a wide redshift range, from $0.22 \leq z \leq 1.01$, making it ideal for studies of evolution of cluster properties. The cluster redshift, velocity dispersion, and other properties of each cluster are summarized in Table 4, while the velocity histograms for the full sample are shown in the Figure 8, Figure 9, and Figure 10, in Appendix A.

4. DYNAMICAL MASSES

Dynamical information of galaxy clusters offers a unique possibility for estimating the virial mass of these systems through the relationship between the velocity dispersion of galaxy members and the cluster mass. Mass estimates based on simple variations of the virial theorem are biased high by a factor of 10 – 20% compared with masses obtained from the Jeans analysis (Carlberg et al.

Table 2
Spectroscopic redshift of individual lensed galaxies

Cluster Lens	Lensed galaxy ^a	R.A. ^b (J2000)	Dec ^b (J2000)	z ^c	Classification ^d
SDSS J0004–0103	S1.1	00 04 51.59	-01 03 19.8	1.681	3
RCS2 J0034+0225	S1.1	00 34 27.35	+02 25 14.1	2.379	3
–	S1.2	00 34 27.39	+02 25 22.1	2.379	3
RCS2 J0038+0215	S1.1	00 38 55.92	+02 15 48.9	2.817	3
–	S1.2	00 38 55.90	+02 15 56.8	2.817	3
RCS2 J0047+0508	S1.1	00 47 51.12	+05 08 27.7	1.629	2
–	S2.1	00 47 51.47	+05 07 52.1	0.728	3
RCS2 J0052+0433	S1.1	00 52 07.73	+04 33 34.5	1.853	2
–	S2.1	00 52 10.94	+04 33 28.8	1.732	2
–	S2.2	00 52 10.57	+04 33 25.3	1.732	2
RCS2 J0057+0209	S1.1	00 57 27.98	+02 09 26.6	0.775	1
–	S1.2	00 57 27.66	+02 09 27.5	0.775	1
RCS2 J0252–1459	S1.1	02 52 41.74	-14 59 33.2	1.096	3
RCS2 J0309–1437	S1.1	03 09 44.99	-14 37 16.1	1.519	3
–	S2.1	03 09 45.33	-14 37 16.2	1.413	2
RCS2 J0327–1326	S1.1	03 27 26.63	-13 26 15.4	1.701	3
–	S1.2	03 27 27.19	-13 26 54.3	1.701	3
–	S1.3	03 27 28.36	-13 26 15.6	1.701	3
RCS2 J0859–0345	S1.1	08 59 14.30	-03 45 12.5	–	0
RCS2 J1055–0459	S1.1	10 55 36.28	-04 59 41.7	2.804	3
–	S1.2	10 55 35.91	-04 59 38.4	2.804	3
RCS2 J1101–0602	S1.1	11 01 53.95	-06 02 31.3	1.674	3
RCS2 J1108–0456	S1.1	11 08 16.24	-04 56 23.3	1.521	1
–	S2.1	11 08 17.31	-04 56 17.0	1.388	1
SDSS J1111+1408	S1.1	11 11 24.26	+14 09 01.6	2.141	3
RCS2 J1119–0728	S1.1	11 19 12.26	-07 28 14.0	2.062	1
RCS2 J1125–0628	S1.1	11 25 29.21	-06 28 48.9	1.518	1
–	S1.2	11 25 28.96	-06 28 49.8	1.518	1
RCS2 J1250+0244	S1.1	12 50 42.20	+02 44 31.2	2.307	2
RCS2 J1511+0630	S1.1	15 11 44.39	+06 30 31.2	1.295	1
SDSS J1517+1003	S1.1	15 17 03.75	+10 03 32.9	2.239	3
–	S1.2	15 17 03.95	+10 03 25.9	2.239	3
SDSS J1519+0840	S1.1	15 19 30.04	+08 40 05.4	2.371	3
–	S1.2	15 19 30.07	+08 39 53.2	2.371	3
RCS2 J1526+0432	S1.1	15 26 13.94	+04 33 02.0	1.443	3
–	S2.1	15 26 15.73	+04 32 42.7	2.636	2
SDSS J2111–0114	S1.1	21 11 18.91	-01 14 31.9	2.856	3
–	S1.2	21 11 20.22	-01 14 33.0	2.856	3
–	S1.3	21 11 20.40	-01 14 30.8	2.856	3
SDSS J2135–0102	S1.1	21 35 12.08	-01 03 36.7	2.319	3
–	S1.2	21 35 11.46	-01 03 34.3	2.319	3
–	S1.3	21 35 09.94	-01 03 18.0	2.319	3
–	S2.1	21 35 10.17	-01 03 33.8	0.903	3
RCS2 J2147–0102	S1.1	21 47 37.12	-01 02 56.3	2.327	1
RCS2 J2151–0138	S1.1	21 51 26.87	-01 38 41.1	0.835	2
SDSS J2313–0104	S1.1	23 13 54.54	-01 04 56.6	1.845	1
RCS2 J2329–0120	S1.1	23 29 47.18	-01 20 45.4	1.790	2
–	S2.1	23 29 47.87	-01 20 53.6	1.570	3
–	S2.2	23 29 47.74	-01 20 53.6	1.570	3
RCS2 J2329–1317	S1.1	23 29 10.33	-13 17 44.3	1.441	2
–	S1.2	23 29 10.03	-13 17 41.7	1.441	2
RCS2 J2336–0608	S1.1	23 36 20.54	-06 08 38.4	1.295	1
–	S1.2	23 36 20.38	-06 08 33.8	1.295	1

^a Lensed galaxy labels that correspond to the label markers in Figures 11 – 18, in Appendix B. S1.X spectra correspond to the “primary” arcs of each cluster, following the notation in Bayliss et al. (2011b).

^b Coordinates of the lensed galaxies in sexagesimal degrees (J2000).

^c Spectroscopic redshift.

^d Classification of the redshift measurements, as discussed in Section 3.1.

1997) and the caustic technique (Diaferio & Geller 1997). In order to account for this bias and obtain an universal virial scaling relation for massive DM halos, Evrard et al. (2008) studied an ensemble of cold DM simulations in a variety of cosmologies. They concluded that the large majority ($\sim 90\%$) of massive halos ($M_{200} \geq 10^{14} M_{\odot}$) are, on average and in all cosmologies, consistent with a virialized state and obey a power-law relation between one-dimensional DM particle velocity dispersion, σ_{DM} , and halo mass. Accordingly, the mass enclosed within

the virial radius, r_{200} , scales as

$$M_{200} = \frac{10^{15}}{h(z)} \left(\frac{\sigma_{DM}}{\sigma_{15}} \right)^{1/\alpha} M_{\odot}, \quad (1)$$

where $\sigma_{15} = 1082.9 \pm 4.0 \text{ km s}^{-1}$ is the normalization for a halo mass of $10^{15} h^{-1} M_{\odot}$, $\alpha = 0.3361 \pm 0.0026$ is the logarithmic slope, and $h(z) = H(z)/100 \text{ km s}^{-1} \text{ Mpc}^{-1}$ is the normalized Hubble parameter at redshift z for a flat universe.

Table 3

The VLT/Magellan spectroscopic redshift catalog of the cluster members reported in this work

Cluster name ^a	R.A. ^b (J2000)	Dec. ^b (J2000)	z^c
RCS2 J0004–0103	1.16403723	-1.03105652	0.5175
RCS2 J0004–0103	1.18741393	-1.03259635	0.5172
RCS2 J0004–0103	1.21820974	-1.07451379	0.5107
RCS2 J0004–0103	1.25292516	-1.05631912	0.5148
RCS2 J0004–0103	1.26846313	-1.05855823	0.5103
RCS2 J0004–0103	1.26440382	-1.06821537	0.5157
RCS2 J0004–0103	1.26328409	-1.07717276	0.5162
RCS2 J0004–0103	1.17243600	-1.03644502	0.5140
RCS2 J0004–0103	1.17733526	-1.03910434	0.5127
RCS2 J0034+0225	8.60755825	2.47035551	0.3845

Note. — Table 3 is published in its entirety in the machine-readable format. A portion is shown here for guidance regarding its form and content. The full table contains 4 columns and 1004 redshifts.

^a Cluster identifier.

^b Coordinates of the cluster member galaxies in decimal degrees (J2000).

^c Spectroscopic redshift.

Computing dynamical mass from Eq. 1 requires a good understanding of the relationship between the DM particle velocity dispersion of cluster halos and the velocity dispersion of cluster members, σ_c , often parameterized by the velocity bias $b_v = \sigma_c/\sigma_{DM}$. Previous studies based on simulation have shown that this velocity bias assumes values in the range $b_v \sim 1.0 - 1.3$ (Diemand et al. 2004; Colín et al. 2000; Ghigna et al. 2000), although more recent simulations have indicated that the way in which subhalos are tracked and defined affects the resulting velocity bias predictions (Evrard et al. 2008; White et al. 2010). In particular, subhalos that are treated in this way show no evidence of a possible velocity bias, i.e. $b_v \sim 1.0$. For consistency with these latest simulation results, we assume that galaxies are unbiased tracers of the total cluster mass (adopting $b_v = 1$), and derive dynamical masses of all clusters in our sample by applying Eq. 1. The mass range of our SL sample goes from $5 \times 10^{13} h_{70}^{-1} M_\odot$ to $1.9 \times 10^{15} h_{70}^{-1} M_\odot$. This wide mass range puts our sample in an excellent position to study relationships between the halo mass of galaxy clusters and their properties, such as the concentration, ellipticity, triaxiality, etc.

The uncertainties in the mass estimates include both the systematic and statistical errors introduced by the $\sigma_{DM} - M_{200}$ scaling relation, redshift measurements, and velocity dispersion estimates. The potential biases due to the lack of cluster members and line-of-sight projection together with other effects that might affect our measurements will be analyzed in the next section. The mass estimates and their respective errors are reported in the Table 4.

5. DISCUSSION

Before we discuss the implications of these results we explore some effects that may affect our measurements. The most important factors that might bias the results are the presence of substructure in our clusters, the region where cluster members were selected for the spectroscopic follow-up, and the final number of confirmed members used in the velocity dispersion estimates. The

other biases are the result of assumptions made about the isotropy of galaxy orbits and the nature of the lensing cluster population itself.

5.1. Substructure

Numerical and observational studies have shown that a significant fraction of galaxy clusters contain substructure, which is frequently attributed to the active merging histories of massive halos (White et al. 2010; Battaglia et al. 2012). However, this does not affect the velocity dispersion measurements when the clusters under consideration have a uni-modal velocity distribution (Girardi et al. 1997), i.e. when the substructure is only marginal and not of comparable size to the cluster itself (having $< 10\%$ of the cluster members in an average extension of ~ 0.2 Mpc h^{-1}).

In order to search for substructure in our sample we apply the DS test (Dressler & Shectman 1988) to those clusters with high enough number of member galaxies ($N_{\text{mem}} \gtrsim 20$). The DS test has been proven as one of the most sensitive tests for dynamical substructure (Pinkney et al. 1996) and widely used in the literature (Cen 1997; Knebe & Müller 2000; White et al. 2010; Hou et al. 2009a, 2012; Sifón et al. 2013). The test is based on the detection of localized subgroups of galaxies that deviate from the global distribution of velocities by using the substructure estimator $\Delta = \sum_i \delta_i$, with

$$\delta_i^2 = \left(\frac{N_{\text{local}} + 1}{\sigma_c^2} \right) [(\bar{v}_i - \bar{v})^2 + (\sigma_i - \sigma_c)^2], \quad (2)$$

where \bar{v}_i and σ_i correspond to the mean and standard deviation of the velocity distribution of the N_{local} members closest to the i th member (included), while \bar{v} and σ_c correspond to the mean velocity and velocity dispersion using all available cluster members, respectively. The null hypothesis of the DS test is no correlation between position and velocity, i.e. the mean velocity and dispersion should be the same locally as globally (within counting statistic). The P -values for the DS test are calculated as in Hou et al. (2012); by comparing the observed substructure estimator Δ_{obs} to the shuffled values Δ_{shuffled} , which are computed by randomly shuffling the observed velocities and reassigning these values to the member positions via 1000 Monte Carlo (MC) simulations, and by taking $N_{\text{local}} = \sqrt{N_{\text{mem}}}$. The P -values are given by

$$P = \sum (\Delta_{\text{shuffled}} - \Delta_{\text{obs}}) / n_{\text{shuffle}}, \quad (3)$$

where n_{shuffle} is the number of MC simulations used to compute the probability. The statistic of the DS test is performed by 100 realizations of the process above, with the central value given by the mean of the P -values distribution and the uncertainties given by the upper and lower 68% confidence intervals. One can see from Eq. 3 that clusters with significant substructure will have low P -values, since it is unlikely to obtain Δ_{obs} randomly. We have therefore set the threshold for substructure detection to a significance level (s.l.) of 0.05 within uncertainties, where false detections are not expected given the size of our sample (Pinkney et al. 1996; Sifón et al. 2013). The results are listed in Table 4. There are 10 out of 24 clusters ($N_{\text{mem}} \gtrsim 20$) that have

Table 4
Summary of dynamical properties of the SL-selected galaxy clusters

Name	R.A. ^a (J2000)	Dec ^a (J2000)	z	N_{mem}	σ_c ^b [km s ⁻¹]	M_{200} [$h_{70}^{-1}10^{14}M_{\odot}$]	r_{200} [$h_{70}^{-1}Mpc$]	P -v (DS) ^c	P -v (KS) ^d
SDSS J0004–0103 ^e	00 04 52.001	–01 03 16.58	0.5144	9	502 ± 144	1.10 ± 0.71	0.83 ± 0.23	–	–
RCS2 J0034+0225	00 34 28.134	+02 25 22.34	0.3842	26	713 ± 179	3.37 ± 2.19	1.26 ± 0.31	0.10 ^{+0.06} _{–0.03}	0.25 ^{+0.08} _{–0.10}
RCS2 J0038+0215 ^g	00 38 55.898	+02 15 52.35	0.6959	20	778 ± 105	3.63 ± 1.47	1.14 ± 0.16	0.04 ^{+0.10} _{–0.02}	0.52 ^{+0.14} _{–0.23}
RCS2 J0047+0508	00 47 50.787	+05 08 20.02	0.4286	50	738 ± 94	3.64 ± 1.40	1.27 ± 0.16	0.24 ^{+0.06} _{–0.06}	0.79 ^{+0.05} _{–0.15}
RCS2 J0052+0433	00 52 10.352	+04 33 33.31	0.7248	24	618 ± 166	1.80 ± 1.17	0.89 ± 0.24	0.12 ^{+0.06} _{–0.04}	0.31 ^{+0.26} _{–0.18}
RCS2 J0057+0209 ^g	00 57 27.869	+02 09 33.98	0.2928	19	940 ± 160	8.07 ± 4.11	1.74 ± 0.30	0.09 ^{+0.08} _{–0.05}	0.31 ^{+0.17} _{–0.20}
RCS2 J0252–1459 ^g	02 52 41.474	–14 59 30.38	0.2646	36	931 ± 121	8.00 ± 3.10	1.76 ± 0.23	0.05 ^{+0.07} _{–0.03}	0.54 ^{+0.11} _{–0.16}
RCS2 J0309–1437 ^{f,g}	03 09 44.096	–14 37 34.38	0.8079	27	620 ± 56	1.74 ± 0.47	0.86 ± 0.07	0.02 ^{+0.06} _{–0.01}	0.04 ^{+0.12} _{–0.02}
RCS2 J0327–1326 ^g	03 27 27.174	–13 26 22.90	0.5633	44	1029 ± 122	9.04 ± 3.20	1.63 ± 0.19	0.05 ^{+0.05} _{–0.02}	0.49 ^{+0.09} _{–0.14}
RCS2 J0859–0345 ^e	08 59 14.486	–03 45 14.63	0.6483	8	912 ± 555	6.01 ± 3.90	1.37 ± 0.83	–	–
RCS2 J1055–0459	10 55 35.647	–04 59 41.60	0.6076	40	720 ± 68	3.04 ± 0.86	1.11 ± 0.10	0.21 ^{+0.05} _{–0.08}	0.89 ^{+0.04} _{–0.32}
RCS2 J1101–0602 ^e	11 01 54.093	–06 02 32.02	0.4861	8	573 ± 201	1.66 ± 1.09	0.96 ± 0.33	–	–
RCS2 J1108–0456	11 08 16.835	–04 56 37.62	0.4088	51	643 ± 52	2.46 ± 0.60	1.11 ± 0.09	0.12 ^{+0.06} _{–0.04}	0.89 ^{+0.07} _{–0.19}
SDSS J1111+1408 ^g	11 11 24.483	+14 08 50.82	0.2204	20	908 ± 121	7.59 ± 3.01	1.74 ± 0.23	0.08 ^{+0.10} _{–0.04}	0.74 ^{+0.10} _{–0.29}
RCS2 J1119–0728 ^e	11 19 11.925	–07 28 17.51	1.0128	4	670 ± 338	1.93 ± 1.26	0.81 ± 0.41	–	–
RCS2 J1125–0628	11 25 28.940	–06 28 39.04	0.4746	33	738 ± 127	3.56 ± 1.81	1.23 ± 0.21	0.16 ^{+0.03} _{–0.04}	0.15 ^{+0.09} _{–0.08}
RCS2 J1250+0244	12 50 41.890	+02 44 26.57	0.6902	33	636 ± 96	2.00 ± 0.90	0.93 ± 0.14	0.15 ^{+0.06} _{–0.06}	0.31 ^{+0.05} _{–0.11}
RCS2 J1511+0630 ^e	15 11 44.681	+06 30 31.79	0.5513	15	444 ± 210	0.74 ± 0.49	0.71 ± 0.33	–	–
SDSS J1517+1003	15 17 02.587	+10 03 29.27	0.6435	57	789 ± 88	3.91 ± 1.30	1.19 ± 0.13	0.29 ^{+0.10} _{–0.04}	0.49 ^{+0.12} _{–0.09}
SDSS J1519+0840 ^g	15 19 31.213	+08 40 01.43	0.3177	49	1177 ± 91	15.57 ± 3.61	2.14 ± 0.17	0.04 ^{+0.08} _{–0.02}	0.35 ^{+0.07} _{–0.10}
RCS2 J1526+0432	15 26 14.914	+04 32 48.01	0.6341	30	735 ± 89	3.19 ± 1.16	1.11 ± 0.13	0.18 ^{+0.07} _{–0.09}	0.43 ^{+0.08} _{–0.12}
SDSS J2111–0114	21 11 19.307	–01 14 23.95	0.6361	46	1014 ± 88	8.29 ± 2.14	1.53 ± 0.13	0.21 ^{+0.05} _{–0.11}	0.88 ^{+0.06} _{–0.16}
SDSS J2135–0102 ^g	21 35 12.040	–01 02 58.27	0.3272	93	1234 ± 83	17.86 ± 3.60	2.23 ± 0.16	0.03 ^{+0.06} _{–0.02}	0.31 ^{+0.19} _{–0.14}
RCS2 J2147–0102	21 47 37.172	–01 02 51.93	0.8801	26	386 ± 79	0.40 ± 0.24	0.51 ± 0.10	0.11 ^{+0.05} _{–0.04}	0.16 ^{+0.08} _{–0.10}
RCS2 J2151–0138	21 51 25.950	–01 38 50.14	0.3160	53	1063 ± 99	11.57 ± 3.20	1.94 ± 0.19	0.14 ^{+0.08} _{–0.06}	0.91 ^{+0.05} _{–0.19}
SDSS J2313–0104	23 13 54.514	–01 04 48.46	0.5271	26	681 ± 112	2.70 ± 1.33	1.10 ± 0.19	0.10 ^{+0.07} _{–0.04}	0.25 ^{+0.07} _{–0.11}
RCS2 J2329–1317 ^g	23 29 09.528	–13 17 49.26	0.3910	80	1019 ± 102	9.73 ± 2.91	1.79 ± 0.17	0.03 ^{+0.06} _{–0.02}	0.31 ^{+0.05} _{–0.09}
RCS2 J2329–0120	23 29 47.782	–01 20 46.89	0.5311	40	1009 ± 109	8.70 ± 2.80	1.63 ± 0.17	0.15 ^{+0.04} _{–0.05}	0.89 ^{+0.03} _{–0.15}
RCS2 J2336–0608 ^g	23 36 20.838	–06 08 35.81	0.3924	36	1041 ± 113	10.43 ± 3.37	1.81 ± 0.20	0.06 ^{+0.05} _{–0.03}	0.88 ^{+0.04} _{–0.24}

^a Coordinates are BCG centroids in sexagesimal degrees (J2000).

^b The rest-frame velocity dispersion of the clusters.

^c P -values of the DS test. The uncertainties are given by the upper and lower 68% confidence intervals. The threshold for substructure detection is set to a s.l. of 0.05 within uncertainties.

^d P -values of the KS test. The uncertainties are given by the upper and lower 68% confidence intervals. The threshold for rejecting the null hypothesis is set to a s.l. of 0.05 within uncertainties.

^e Systems with few spectroscopically confirmed cluster members, $N_{mem} \lesssim 20$. Their velocity dispersion and mass measurements represent only a first guess and should not be considered as the final estimates.

^f The null hypothesis of the KS test is rejected, suggesting that the velocity data of this system is not consistent with a uni-modal distribution. Its velocity dispersion and mass measurements represent only a first guess and should not be considered as the final estimates.

^g Systems showing signs of dynamical substructure based on DS test results.

rejected the null hypothesis, indicating signs of dynamical substructure which is consistent with previous optical and X-ray studies of local clusters (Girardi et al. 1997; Schuecker et al. 2001). However, high values of Δ might also be obtained when the velocities are shuffled, leading to a higher probability-to-exceed or a lower significance detection of substructure, resulting in erroneous assumptions that are consistent with no substructure (White et al. 2010). Furthermore, the DS test (and almost all substructure indicators) is highly viewing-angle dependent which complicates the inferences about the dynamical state of the clusters.

Since substructure does not affect the velocity dispersion measurements when the clusters under consideration have a uni-modal velocity distribution (Girardi et al. 1997; Evrard et al. 2008; Sifón et al. 2013), we apply the Kolmogorov-Smirnov test (KS; Hou et al. 2009b, and references therein) to those clusters in our sample with

$N_{mem} \gtrsim 20$, to corroborate whether their velocity distributions are consistent with a Gaussian distribution. The KS test is a non-parametric hypothesis test based on the *supremum* statistics that measures the distance between the empirical distribution function (EDF) of a sample and the cumulative distribution function (CDF) of a chosen reference distribution. We set the mean and variance of the reference distribution to the mean velocity and velocity dispersion squared of each cluster, respectively. The statistic of the KS test is calculated by 5000 bootstrapped realizations of the velocity data of each cluster, with the final probability given by the mean of the P -values distribution and the uncertainties given by the upper and lower 68% confidence intervals. The threshold for rejecting the null hypothesis, that the sample is drawn from the reference distribution, is set to a s.l. of 0.05 within uncertainties. The velocity distributions of 23 out of 24 clusters (with $N_{mem} \gtrsim 20$) show high

P -values, suggesting that the deviation between the velocity data of these clusters and a Gaussian distribution is smaller than one would expect to arise from two different distributions. We therefore assume that the velocity distributions of these 23 SL clusters are uni-modal; consequently, we can conclude that their velocity dispersion measurements are robust and that their mass estimates are representative of their total masses, i.e. Eq. 1 is valid for this subset. The results are listed in Table 4. For completeness, we also apply a Gaussian fit to the binned data of the velocity histograms of these clusters. In all cases, the best-fitting Gaussian parameters are consistent with the mean velocity and velocity dispersion squared within 1σ , although the fit usually depends on the choice of the bin width. Their velocity histograms together with their respective Gaussian fits are shown in Figure 8 and Figure 9, in Appendix A.

RCS2 J0309–1437 is the only system in our sample (with $N_{\text{mem}} \gtrsim 20$) where the null hypothesis of the KS test is rejected, suggesting that its velocity data is not consistent with a uni-modal distribution. Nonetheless, we list its velocity dispersion and virial mass in table 4, along with the estimates for five systems with relatively few spectroscopically confirmed cluster members ($\langle N_{\text{mem}} \rangle \sim 10$). It should be noted that the measurements for these six systems represent only a first guess and should not be considered as the final estimates. The velocity histograms for these clusters are shown in Figure 10, in Appendix A.

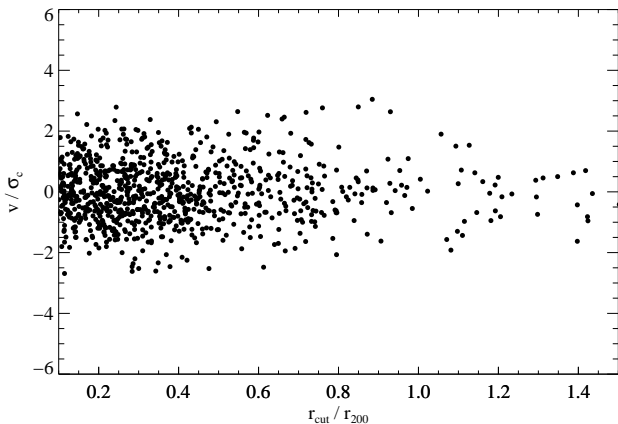


Figure 6. The stacked analysis of our 29 galaxy clusters. The peculiar velocity of each galaxy normalized by the velocity dispersion σ_c of the corresponding cluster versus the cluster-centric distance normalized by r_{200} for each cluster is shown.

5.2. Region of cluster members

Observational and theoretical studies have shown that velocity dispersion profiles are flat from $\sim 0.6 - 0.8 r_{200}$ outward (Fadda et al. 1996; Biviano & Girardi 2003; Faltenbacher & Diemand 2006), and highly biased in the innermost regions of the clusters ($\sim 0.2 r_{200}$). Hence, estimating the effect of this potential sampling bias requires the knowledge of the virial radius for each cluster and also its projected angular size on the sky. We derive the virial radius of all clusters in our sample by assum-

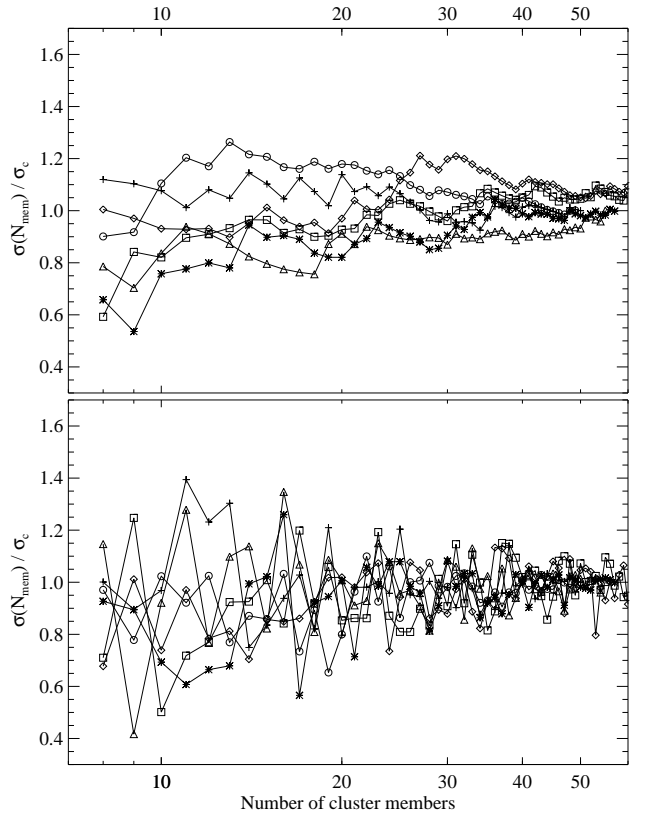


Figure 7. The top panel shows the line-of-sight velocity dispersion versus the number of cluster members ordered by luminosity (from highest to lowest) for 6 clusters from our SL lensing sample with more than 49 member galaxies. The bottom panel shows the line-of-sight velocity dispersion but with the inclusion of randomly selected N_{mem} member galaxies. In both panels the resultant line-of-sight velocity dispersion has been normalized by the total dispersion of the corresponding cluster, σ_c . In both cases the scatter is symmetric about the ratio of 1 when $N_{\text{mem}} \gtrsim 20$, indicating that the estimates are mainly affected by the lack of galaxy tracers rather than by dynamical friction. The cluster RCS2 J0047+0507 is represented by “+”; RCS2 J1517+1003 by “*”; RCS2 J1519+0840 by “o”; SDSS J2135–0102 by “o”; RCS2 J2151–0138 by “Δ”; and the cluster RCS2 J2329–1317 by “□”.

ing spherical symmetry²⁰ and using the previous results of M_{200} (i.e. $M_{200} = 200\rho_c \times 4\pi r_{200}^3/3$), resulting in a median virial radius of $r_{200} = 0.88 \text{ Mpc h}^{-1}$ that corresponds to an angular size on the sky of $\theta_{r_{200}} = 3.5'$. Since our field of view has an average angular radius of $\sim 3.2'$ from the cluster centers, we are sampling cluster galaxies till approximately $0.9 r_{200}$ of the clusters. Therefore, the field restriction should not bias our results because the flatness of the velocity dispersion profiles begins to smaller radii. Furthermore, since we are mainly sampling cluster members on average within $\sim 0.9 r_{200}$ (Figure 6), the probability to include interlopers is approximately 30% lower than for sampling till twice r_{200} (White et al. 2010; Saro et al. 2013).

5.3. Number of cluster members

The number of cluster members plays a decisive role in the analysis of dynamical cluster properties and velocity dispersion measurements (Biviano et al. 2006;

²⁰ The virial radii of our cluster sample are listed in Table 4

Wojtak & Lokas 2010). White et al. (2010), using high resolution N-body simulations, studied the stability of the cluster velocity dispersion as a function of the number of subhalos used to estimate it. They found that the results are generally stable once $\gtrsim 50$ subhalos are included; however, there is an intrinsic scatter of $\sim 10\%$ between the line-of-sight velocity dispersion and the DM halo velocity dispersion, mainly due to the halo triaxiality. They also found that the line-of-sight velocity dispersion is biased low when a small number of subhalos is used (increasing the scatter), but estimates with $N_{\text{mem}} \gtrsim 20$ tend asymptotically to the true velocity dispersion of clusters. Indeed, there is a general consensus in the literature that identifying on the order of 20 member galaxies is sufficient to derive the velocity dispersion of clusters (Beers et al. 1990; Aguerri & Sánchez-Janssen 2010; Hou et al. 2012), although there could be a $\sim 15\%$ underestimation if only brighter galaxies are used, indicating that dynamical friction of brighter galaxies has a significant impact on the measured velocity dispersion (Old et al. 2013; Saro et al. 2013).

As mentioned in §3, we have recovered a total of 1004 spectroscopically confirmed cluster members, which gives us an average of $\langle N_{\text{mem}} \rangle \sim 35$ member galaxies per cluster. Therefore, we could assume that our estimates represent the “true” line-of-sight velocity dispersion of our clusters based on the studies above. However, we need to explore if these measurements are affected by dynamical friction since our spectroscopic strategy was to prioritize brighter galaxies ahead of fainter ones. In order to probe this possible systematic bias, we analyze the behavior of the velocity dispersion as a function of the number of brighter cluster members of 6 clusters from our sample with $N_{\text{mem}} \gtrsim 50$. We rank the member galaxies according to their absolute r' -band magnitude and calculate the line-of-sight velocity dispersion using the brightest galaxies from $N_{\text{mem}} = 8$ to $N_{\text{mem}} = N_{\text{total}}$. We plot the resultant velocity dispersions $\sigma(N_{\text{mem}})$ in Figure 7 (top panel), normalized by the final dispersion σ_c , obtained using all available cluster members. As showed by previous studies, the scatter between $\sigma(N_{\text{mem}})$ and σ_c increases considerably for a lower number of cluster members ($N_{\text{mem}} \lesssim 15$), showing a clear underestimation of σ when $N_{\text{mem}} \lesssim 10$. For measurements using $N_{\text{mem}} \gtrsim 20$, the scatter is almost symmetric, i.e. the bias introduced by using only a fraction of the total number of member galaxies may underestimate or overestimate the “true” line-of-sight velocity dispersions, and whether the bias is from above or below depends upon the cluster under consideration (e.g. White et al. 2010). Therefore, estimates using $N_{\text{mem}} \gtrsim 20$ are only slightly affected by dynamical friction; pointing out that the most likely effect that is affecting our measurements should be associated to the lack of galaxy tracers.

To corroborate these conclusions, we repeat the previous process but choosing the member galaxies randomly with respect to their absolute r -band magnitude. The results are shown in the bottom panel of Figure 7. In this figure one can easily see that for estimates using $N_{\text{mem}} \gtrsim 20$, the scatter around the “true” line-of-sight velocity dispersion is symmetric and similar to the scatter obtained when cluster members are sorted by their brightness. Therefore, we can assume that velocity dispersion estimates are mainly affected by the lack of clus-

ter members rather than by dynamical friction. Indeed, in both cases of Figure 7, the average scatter is of the order of $\sim 10\%$ when N_{mem} is equal to the average number of cluster members, i.e. $N_{\text{mem}} = \langle N_{\text{mem}} \rangle = 35$. It is to be noted that this 10% of scatter should be considered as the lower scatter that we should include in our velocity dispersion estimates in order to take into account the lack of cluster members. But we leave this discussion for future observational and simulation studies, where we could compare results from a larger number of cluster members with specific simulations for the SL galaxy cluster population.

5.4. Line-of-sight effect

It is well known that virialized halos that host galaxy clusters are triaxial (Thomas & Couchman 1992; Warren et al. 1992; Jing & Suto 2002), with the major axis approximately twice as long as the minor axes which are approximately equal in size. This prolate shape could potentially lead to a bias in the velocity dispersion estimates because the velocity tensor is quite anisotropic and generally well aligned with the inertia tensor, with a typical misalignment angle of $\sim 30^\circ$ (Tormen et al. 1997; Kasun & Evrard 2005; White et al. 2010). In other words, viewing along the major axis may contribute to a higher velocity dispersion, while the two minor axes to lower values; hence, the final measurements depend significantly on the chosen line-of-sight. In fact, numerical simulations have shown that, although the 3D velocity dispersion of DM particles within r_{200} is well correlated with M_{200} and the galaxies show little velocity bias compared to the DM particles, the line-of-sight velocity dispersions show a considerably larger scatter and the mass estimates from these measurements are biased with respect to the true values (Evrard et al. 2008; White et al. 2010; Saro et al. 2013).

Studies based on simulations of SL halos have shown that the most effective strong lenses are not more triaxial than the general halo population (Hennawi et al. 2007; Meneghetti et al. 2010); however, they are more likely to have their major axes aligned along the line-of-sight. Therefore, we should assume that the velocity dispersion estimates for a sample of SL-selected clusters will be biased high with respect to the velocity dispersions measured for clusters that are randomly oriented on the sky. However, the intrinsic misalignment between the halo positional ellipsoid and the velocity tensor introduces an element of randomization in the orientation of the velocity tensor with respect to the line-of-sight that reduces the impact of the orientation bias. Specific predictions for the magnitude of this bias require the convolution of the probability distributions for the position orientation angle of the SL-selected clusters with their velocity principal axes. Since we do not have these probability distributions, we leave this additional correction for future analyses and as in the previous section, we do not include this extra uncertainty in our estimates. But it is important to note that our line-of-sight velocity dispersion measurements should have, at least, a scatter of the same order as found by White et al. (2010) for the normal cluster population, i.e. a scatter of the order of $\sim 10\%$ between the line-of-sight and 3D velocity dispersions.

6. SUMMARY AND CONCLUSIONS

We have conducted a large spectroscopic follow-up program of 29 SL-selected galaxy clusters discovered in the RCS-2 survey. Our spectroscopic analysis has revealed the nature of 52 gravitational arcs present in the core of our galaxy clusters, which correspond to 35 background sources at high-redshifts that are clearly distorted by the gravitational potential of these clusters. These lensed galaxies span a wide redshift range of $0.8 \leq z \leq 2.9$, with a median redshift of $z_s = 1.8 \pm 0.1$, that matches the expectations. This dataset extends the number of galaxy clusters with spectroscopic confirmation of their SL features that are available to perform lensing reconstructions of their mass distribution, especially at $z \gtrsim 0.2$.

This campaign has also yielded a total of 1004 spectroscopically confirmed cluster members that gives an average of $\langle N_{\text{mem}} \rangle \sim 35$ member galaxies per cluster. These data allow us to obtain robust redshifts for each cluster and measure velocity dispersions with relatively high confidence level, which are translated into dynamical masses by using the [Evrard et al. \(2008\)](#) $\sigma_{DM} - M_{200}$ scaling relation. The redshift and mass ranges of our SL sample are distributed from $0.22 \leq z \leq 1.01$ and $5 \times 10^{13} \leq M_{200}/h_{70}^{-1} M_{\odot} \leq 1.9 \times 10^{15}$, respectively. These wide redshift and mass ranges allow diverse kinds of studies: from the analysis of the relationship between the concentration of the cluster halos and their masses to studies of galaxy evolution in cluster environments.

We have analyzed some effects that could affect our velocity dispersion measurements, such as the presence of substructure in our clusters, the region where cluster members were selected, the final number of confirmed members, and the line-of-sight effects. Our primary conclusions are:

- We found that 10 out of 24 of our clusters, where analysis is possible, show signs of dynamical substructure, which is consistent with previous optical and X-ray studies of local clusters. The velocity distributions of 23 of these clusters are consistent with a uni-modal distribution and we therefore assumed that [Eq. 1](#) is applicable to these SL clusters in our sample.
- We sampled cluster member galaxies within the inner $\sim 0.9 r_{200}$ of the clusters, which did not bias our results due to the flatness of the velocity dispersion profiles from $\sim 0.8 r_{200}$. Furthermore, since we mainly sampled cluster members within the virial radius, the probability to include interlopers is approximately 30% lower than for sampling up to twice r_{200} ([Old et al. 2013](#); [Saro et al. 2013](#)).
- We have found that using $N_{\text{mem}} \gtrsim 20$, our velocity dispersion estimates are mainly affected by the lack of galaxy tracers rather than by dynamical friction. We found that in both cases, sorting the cluster members by their brightness or randomly, the scatter is symmetric and of the order of $\sim 10\%$ when $N_{\text{mem}} = \langle N_{\text{mem}} \rangle = 35$. However, it is only a first guess of the magnitude of this potential bias. A better understanding of this effect needs deeper studies of the galaxy kinematics in SL clusters.

Summing up, we have found that our velocity dispersion measurements should be affected by the lack of cluster members as well as by the scatter between the line-of-sight and 3D velocity dispersion. However, specific predictions for the magnitude of these biases require an improvement in both simulation and observational studies, with larger simulations oriented to the SL galaxy cluster population and more spectroscopic information of the cluster members. Even though our measurements may be biased or may have large uncertainties, which are translated into large errors in the mass estimates, they serve as a base for a better understanding of the SL cluster properties. Furthermore, these dynamical masses can be used as *priors* for mass reconstruction studies, that combined with SL signatures yield one of the most robust measurements of the mass distribution of SL clusters.

A complete characterization of the properties and biases of this population is crucial for taking full advantage of future SL samples coming from a new era of large area deep imaging surveys (e.g. PanSTARRS, LSST, DES). The data and analysis presented in this work represent the first steps in this direction and also pave the way for multi-wavelength studies, i.e. when SL information is combined with WL, dynamical masses, X-ray, and SZE data. These kinds of studies will allow us to quantify the biases between the different observable masses in order to fully exploit the additional information provided by SL signatures, which can then be intelligently applied to scaling relations and mass estimates for the general cluster population.

M. Carrasco gives particular thanks to Matthias Bartelmann, Matteo Maturi, Agnese Fabris, Jorge Gorzález, and Cristobal Sifón for useful discussions and collaborations in this work. M. Carrasco's research is supported by the Transregional Collaborative Research Centre TRR 33. M. Carrasco acknowledges the support of ESO through the ESO Studentship and DAA through the PUC-HD Graduate Exchange Fellowship. We thank to ESO and its support staff for the implementation of the Programmes 081.A-0561, 083.A-0491, and 084.A-0317. Support for L.F. Barrientos and T. Anguita is provided by the Ministry of Economy, Development, and Tourism's Millennium Science Initiative through grant IC120009, awarded to The Millennium Institute of Astrophysics, MAS. L. F. Barrientos' research is supported by proyecto FONDECYT 1120676. T. Anguita acknowledges support by proyecto FONDECYT 11130630. DGG acknowledges financial support from the National Research Foundation (NRF) of South Africa.

REFERENCES

- Abazajian, K. N., Adelman-McCarthy, J. K., Agüeros, M. A., Allam, S. S., Allende Prieto, C., An, D., Anderson, K. S. J., Anderson, S. F., et al. 2009, *ApJS*, 182, 543 [[ADS](#)]
 Aguerri, J. A. L. & Sánchez-Janssen, R. 2010, *A&A*, 521, A28 [[ADS](#)]
 Anguita, T., Barrientos, L. F., Gladders, M. D., Faure, C., Yee, H. K. C., & Gilbank, D. G. 2012, *ApJ*, 748, 129 [[ADS](#)]
 Appenzeller, I., Fricke, K., Fürtig, W., Gässler, W., Häfner, R., Harke, R., Hess, H.-J., Hummel, W., et al. 1998, *The Messenger*, 94, 1 [[ADS](#)]
 Bartelmann, M. 2010, *Classical and Quantum Gravity*, 27, 233001 [[ADS](#)]

- Bartelmann, M., Huss, A., Colberg, J. M., Jenkins, A., & Pearce, F. R. 1998, *A&A*, 330, 1 [ADS]
- Battaglia, N., Bond, J. R., Pfrommer, C., & Sievers, J. L. 2012, *ApJ*, 758, 74 [ADS]
- Bayliss, M. B. 2012, *ApJ*, 744, 156 [ADS]
- Bayliss, M. B., Gladders, M. D., Oguri, M., Hennawi, J. F., Sharon, K., Koester, B. P., & Dahle, H. 2011a, *ApJ*, 727, L26 [ADS]
- Bayliss, M. B., Hennawi, J. F., Gladders, M. D., Koester, B. P., Sharon, K., Dahle, H., & Oguri, M. 2011b, *ApJS*, 193, 8 [ADS]
- Bayliss, M. B., Wuyts, E., Sharon, K., Gladders, M. D., Hennawi, J. F., Koester, B. P., & Dahle, H. 2010, *ApJ*, 720, 1559 [ADS]
- Beers, T. C., Flynn, K., & Gebhardt, K. 1990, *AJ*, 100, 32 [ADS]
- Biviano, A. & Girardi, M. 2003, *ApJ*, 585, 205 [ADS]
- Biviano, A., Murante, G., Borgani, S., Diaferio, A., Dolag, K., & Girardi, M. 2006, *A&A*, 456, 23 [ADS]
- Bleem, L. E., Stalder, B., de Haan, T., Aird, K. A., Allen, S. W., Applegate, D. E., Ashby, M. L. N., Bautz, M., et al. 2015, *ApJS*, 216, 27 [ADS]
- Böhringer, H., Schuecker, P., Guzzo, L., Collins, C. A., Voges, W., Cruddace, R. G., Ortiz-Gil, A., Chincarini, G., et al. 2004, *A&A*, 425, 367 [ADS]
- Bouwens, R. J., Illingworth, G. D., Bradley, L. D., Ford, H., Franx, M., Zheng, W., Broadhurst, T., Coe, D., et al. 2009, *ApJ*, 690, 1764 [ADS]
- Bradley, L. D., Bouwens, R. J., Ford, H. C., Illingworth, G. D., Jee, M. J., Benítez, N., Broadhurst, T. J., Franx, M., et al. 2008, *ApJ*, 678, 647 [ADS]
- Burenin, R. A., Vikhlinin, A., Hornstrup, A., Ebeling, H., Quintana, H., & Mescheryakov, A. 2007, *ApJS*, 172, 561 [ADS]
- Cabanac, R. A., Alard, C., Dantel-Fort, M., Fort, B., Gavazzi, R., Gomez, P., Kneib, J. P., Le Fèvre, O., et al. 2007, *A&A*, 461, 813 [ADS]
- Carlberg, R. G., Yee, H. K. C., Ellingson, E., Morris, S. L., Abraham, R., Gravel, P., Pritchett, C. J., Smecker-Hane, T., et al. 1997, *ApJ*, 485, L13 [ADS]
- Cen, R. 1997, *ApJ*, 485, 39 [ADS]
- Coe, D., Zitrin, A., Carrasco, M., Shu, X., Zheng, W., Postman, M., Bradley, L., Koekemoer, A., et al. 2013, *ApJ*, 762, 32 [ADS]
- Colín, P., Klypin, A. A., & Kravtsov, A. V. 2000, *ApJ*, 539, 561 [ADS]
- Dahle, H. 2006, *ApJ*, 653, 954 [ADS]
- Danese, L., de Zotti, G., & di Tullio, G. 1980, *A&A*, 82, 322 [ADS]
- Diaferio, A. & Geller, M. J. 1997, *ApJ*, 481, 633 [ADS]
- Diemand, J., Moore, B., & Stadel, J. 2004, *MNRAS*, 352, 535 [ADS]
- Dressler, A., Bigelow, B., Hare, T., Sutin, B., Thompson, I., Burley, G., Epps, H., Oemler, A., et al. 2011, *PASP*, 123, 288 [ADS]
- Dressler, A., Hare, T., Bigelow, B. C., & Osip, D. J. 2006, in *Society of Photo-Optical Instrumentation Engineers (SPIE) Conference Series*, Vol. 6269, Society of Photo-Optical Instrumentation Engineers (SPIE) Conference Series, 0 [ADS]
- Dressler, A. & Shectman, S. A. 1988, *AJ*, 95, 985 [ADS]
- Erb, D. K., Quider, A. M., Henry, A. L., & Martin, C. L. 2012, *ApJ*, 759, 26 [ADS]
- Evrard, A. E., Bialek, J., Busha, M., White, M., Habib, S., Heitmann, K., Warren, M., Rasia, E., et al. 2008, *ApJ*, 672, 122 [ADS]
- Evrard, A. E., MacFarland, T. J., Couchman, H. M. P., Colberg, J. M., Yoshida, N., White, S. D. M., Jenkins, A., Frenk, C. S., et al. 2002, *ApJ*, 573, 7 [ADS]
- Fadda, D., Girardi, M., Giuricin, G., Mardirossian, F., & Mezzetti, M. 1996, *ApJ*, 473, 670 [ADS]
- Faltenbacher, A. & Diemand, J. 2006, *MNRAS*, 369, 1698 [ADS]
- Geach, J. E., Murphy, D. N. A., & Bower, R. G. 2011, *MNRAS*, 413, 3059 [ADS]
- Ghigna, S., Moore, B., Governato, F., Lake, G., Quinn, T., & Stadel, J. 2000, *ApJ*, 544, 616 [ADS]
- Gilbank, D. G., Gladders, M. D., Yee, H. K. C., & Hsieh, B. C. 2011, *AJ*, 141, 94 [ADS]
- Girardi, M., Escalera, E., Fadda, D., Giuricin, G., Mardirossian, F., & Mezzetti, M. 1997, *ApJ*, 482, 41 [ADS]
- Gladders, M. D., Hoekstra, H., Yee, H. K. C., Hall, P. B., & Barrientos, L. F. 2003, *ApJ*, 593, 48 [ADS]
- Gladders, M. D. & Yee, H. K. C. 2000, *AJ*, 120, 2148 [ADS]
- . 2005, *VizieR Online Data Catalog*, 215, 70001 [ADS]
- Hao, J., McKay, T. A., Koester, B. P., Rykoff, E. S., Rozo, E., Annis, J., Wechsler, R. H., Evrard, A., et al. 2010, *ApJS*, 191, 254 [ADS]
- Hennawi, J. F., Dalal, N., Bode, P., & Ostriker, J. P. 2007, *ApJ*, 654, 714 [ADS]
- High, F. W., Hoekstra, H., Leethochawalit, N., de Haan, T., Abramson, L., Aird, K. A., Armstrong, R., Ashby, M. L. N., et al. 2012, *ApJ*, 758, 68 [ADS]
- Hoekstra, H. & Jain, B. 2008, *Annual Review of Nuclear and Particle Science*, 58, 99 [ADS]
- Horesh, A., Maoz, D., Ebeling, H., Seidel, G., & Bartelmann, M. 2010, *MNRAS*, 406, 1318 [ADS]
- Horne, K. 1986, *PASP*, 98, 609 [ADS]
- Hou, A., Parker, L. C., Harris, W. E., & Wilman, D. J. 2009a, *ApJ*, 702, 1199 [ADS]
- . 2009b, *ApJ*, 702, 1199 [ADS]
- Hou, A., Parker, L. C., Wilman, D. J., McGee, S. L., Harris, W. E., Connelly, J. L., Balogh, M. L., Mulchaey, J. S., et al. 2012, *MNRAS*, 421, 3594 [ADS]
- Jing, Y. P. & Suto, Y. 2002, *ApJ*, 574, 538 [ADS]
- Kasun, S. F. & Evrard, A. E. 2005, *ApJ*, 629, 781 [ADS]
- Knebe, A. & Müller, V. 2000, *A&A*, 354, 761 [ADS]
- Kneib, J.-P. & Natarajan, P. 2011, *A&A Rev.*, 19, 47 [ADS]
- Kurtz, M. J. & Mink, D. J. 1998, *PASP*, 110, 934 [ADS]
- Li, G. L., Mao, S., Jing, Y. P., Mo, H. J., Gao, L., & Lin, W. P. 2006, *MNRAS*, 372, L73 [ADS]
- Limousin, M., Ebeling, H., Richard, J., Swinbank, A. M., Smith, G. P., Jauzac, M., Rodionov, S., Ma, C.-J., Smail, I., Edge, A. C., et al. 2012, *A&A*, 544, A71 [ADS]
- Meneghetti, M., Fedeli, C., Pace, F., Gottlöber, S., & Yepes, G. 2010, *A&A*, 519, A90+ [ADS]
- Morton, D. C. 1991, *ApJS*, 77, 119 [ADS]
- Oguri, M., Hennawi, J. F., Gladders, M. D., Dahle, H., Natarajan, P., Dalal, N., Koester, B. P., Sharon, K., et al. 2009, *ApJ*, 699, 1038 [ADS]
- Okabe, N., Zhang, Y., Finoguenov, A., Takada, M., Smith, G. P., Umetsu, K., & Futamase, T. 2010, *ApJ*, 721, 875 [ADS]
- Old, L., Gray, M. E., & Pearce, F. R. 2013, *MNRAS*, 434, 2606 [ADS]
- Pinkney, J., Roettiger, K., Burns, J. O., & Bird, C. M. 1996, *ApJS*, 104, 1 [ADS]
- Rigby, J. R., Bayliss, M. B., Gladders, M. D., Sharon, K., Wuyts, E., & Dahle, H. 2014, *ApJ*, 790, 44 [ADS]
- Roze, E., Wechsler, R. H., Rykoff, E. S., Annis, J. T., Becker, M. R., Evrard, A. E., Frieman, J. A., Hansen, S. M., et al. 2010, *ApJ*, 708, 645 [ADS]
- Ruel, J., Bazin, G., Bayliss, M., Brodwin, M., Foley, R. J., Stalder, B., Aird, K. A., Armstrong, R., et al. 2014, *ApJ*, 792, 45 [ADS]
- Saro, A., Mohr, J. J., Bazin, G., & Dolag, K. 2013, *ApJ*, 772, 47 [ADS]
- Schuecker, P., Böhringer, H., Reiprich, T. H., & Feretti, L. 2001, *A&A*, 378, 408 [ADS]
- Shapley, A. E., Steidel, C. C., Pettini, M., & Adelberger, K. L. 2003, *ApJ*, 588, 65 [ADS]
- Sifón, C., Menanteau, F., Hasselfield, M., Marriage, T. A., Hughes, J. P., Barrientos, L. F., González, J., Infante, L., et al. 2013, *ApJ*, 772, 25 [ADS]
- Szabo, T., Pierpaoli, E., Dong, F., Pipino, A., & Gunn, J. 2011, *ApJ*, 736, 21 [ADS]
- Thomas, P. A. & Couchman, H. M. P. 1992, *MNRAS*, 257, 11 [ADS]
- Tormen, G., Bouchet, F. R., & White, S. D. M. 1997, *MNRAS*, 286, 865 [ADS]
- Umetsu, K., Medezinski, E., Nonino, M., Merten, J., Postman, M., Meneghetti, M., Donahue, M., et al. 2014, *arXiv*, 1404.1375 [ADS]
- van Uitert, E., Gilbank, D. G., Hoekstra, H., Semboloni, E., Gladders, M. D., & Yee, H. K. C. 2015, *arXiv*, 1506.03817 [ADS]
- Vikhlinin, A., Burenin, R. A., Ebeling, H., Forman, W. R., Hornstrup, A., Jones, C., Kravtsov, A. V., Murray, S. S., et al. 2009, *ApJ*, 692, 1033 [ADS]
- Voges, W., Aschenbach, B., Boller, T., Bräuninger, H., Briel, U., Burkert, W., Dennerl, K., Englhauser, J., et al. 1999, *A&A*, 349, 389 [ADS]

- Voit, G. M. 2005, *Reviews of Modern Physics*, 77, 207 [\[ADS\]](#)
- Warren, M. S., Quinn, P. J., Salmon, J. K., & Zurek, W. H. 1992, *ApJ*, 399, 405 [\[ADS\]](#)
- White, M., Cohn, J. D., & Smit, R. 2010, *MNRAS*, 408, 1818 [\[ADS\]](#)
- White, R. L., Becker, R. H., Helfand, D. J., & Gregg, M. D. 1997, *ApJ*, 475, 479 [\[ADS\]](#)
- Wittman, D., Dell'Antonio, I. P., Hughes, J. P., Margoniner, V. E., Tyson, J. A., Cohen, J. G., & Norman, D. 2006, *ApJ*, 643, 128 [\[ADS\]](#)
- Wojtak, R. & Lokas, E. L. 2010, *MNRAS*, 408, 2442 [\[ADS\]](#)
- Wuyts, E., Barrientos, L. F., Gladders, M. D., Sharon, K., Bayliss, M. B., Carrasco, M., Gilbank, D., Yee, H. K. C., et al. 2010, *ApJ*, 724, 1182 [\[ADS\]](#)
- Wuyts, E., Rigby, J. R., Gladders, M. D., & Sharon, K. 2014, *ApJ*, 781, 61 [\[ADS\]](#)
- Wuyts, E., Rigby, J. R., Sharon, K., & Gladders, M. D. 2012, *ApJ*, 755, 73 [\[ADS\]](#)
- York, D. G., Adelman, J., Anderson, Jr., J. E., Anderson, S. F., Annis, J., et al. 2000, *AJ*, 120, 1579 [\[ADS\]](#)
- Zheng, W., Bradley, L. D., Bouwens, R. J., Ford, H. C., Illingworth, G. D., Benítez, N., Broadhurst, T., Frye, B., et al. 2009, *ApJ*, 697, 1907 [\[ADS\]](#)
- Zheng, W., Postman, M., Zitrin, A., Moustakas, J., Shu, X., Jouvel, S., Host, O., Molino, A., et al. 2012, arXiv, 1204.2305 [\[ADS\]](#)
- Zitrin, A., Broadhurst, T., Umetsu, K., Coe, D., Benítez, N., Ascaso, B., Bradley, L., Ford, H., et al. 2009, *MNRAS*, 396, 1985 [\[ADS\]](#)
- Zitrin, A., Moustakas, J., Bradley, L., Coe, D., Moustakas, L. A., Postman, M., Shu, X., Zheng, W., Benítez, N., Bouwens, R., et al. 2012a, *ApJ*, 747, L9 [\[ADS\]](#)
- Zitrin, A., Rosati, P., Nonino, M., Grillo, C., Postman, M., Coe, D., Seitz, S., Eichner, T., Broadhurst, T., Jouvel, S., et al. 2012b, *ApJ*, 749, 97 [\[ADS\]](#)

APPENDIX
A. VELOCITY HISTOGRAMS

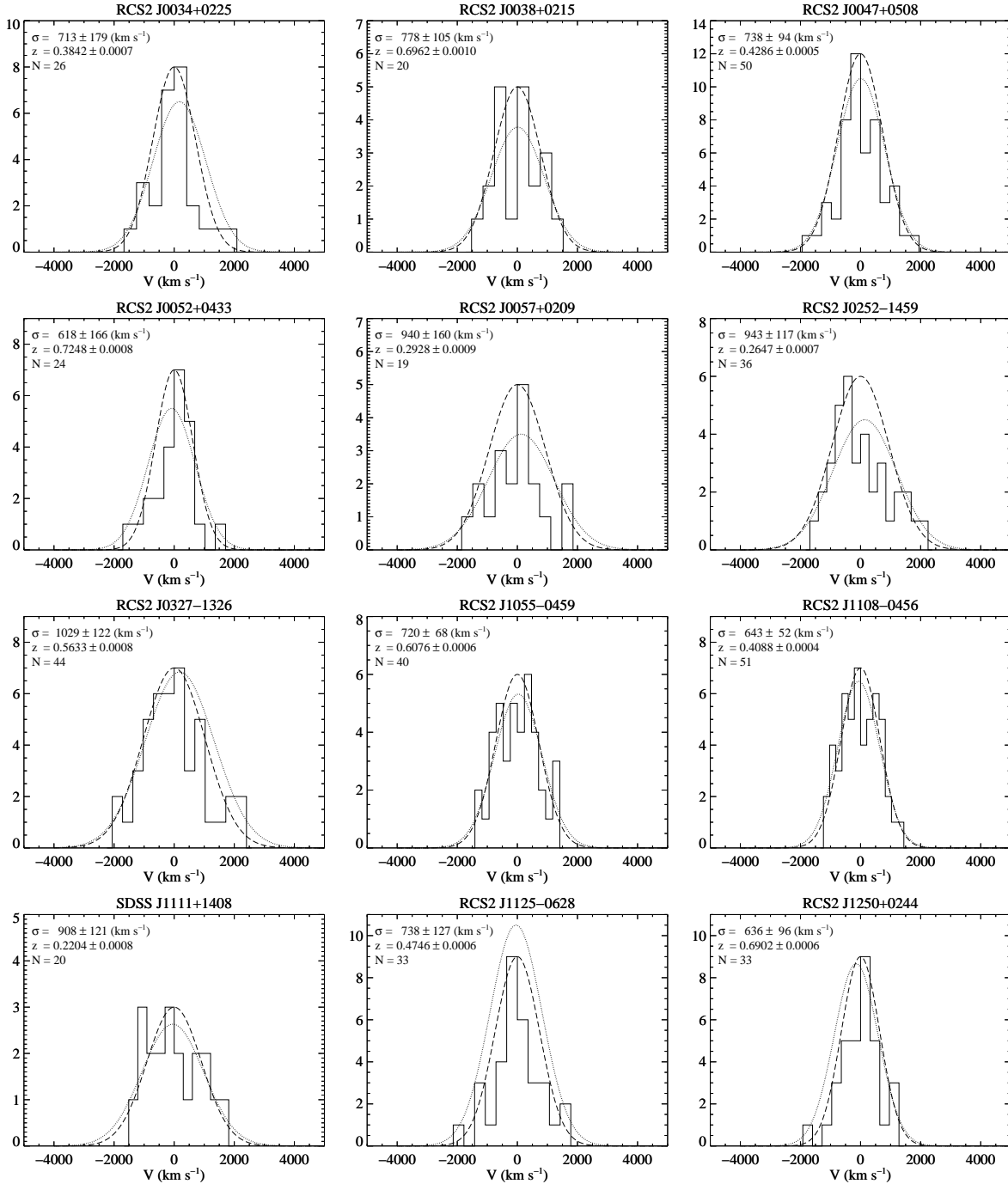


Figure 8. Velocity histograms for 12 out of 23 of our clusters with $N_{\text{mem}} \gtrsim 20$ showing a uni-modal distribution. Each panel is labeled with the name of the corresponding cluster, its rest-frame velocity dispersion, redshift, and the number of cluster members spectroscopically confirmed. Dashed lines correspond to Gaussian (reference) distributions with the mean and variance equal to the mean velocity and velocity dispersion squared of each cluster derived from the bi-weight estimator analysis. Dotted lines correspond to the best-fit Gaussian curves to the velocity histograms, where the best-fitting Gaussian parameters are consistent with the mean velocity and velocity dispersion squared within 1σ . Also, note that the y-axes differ between plots.

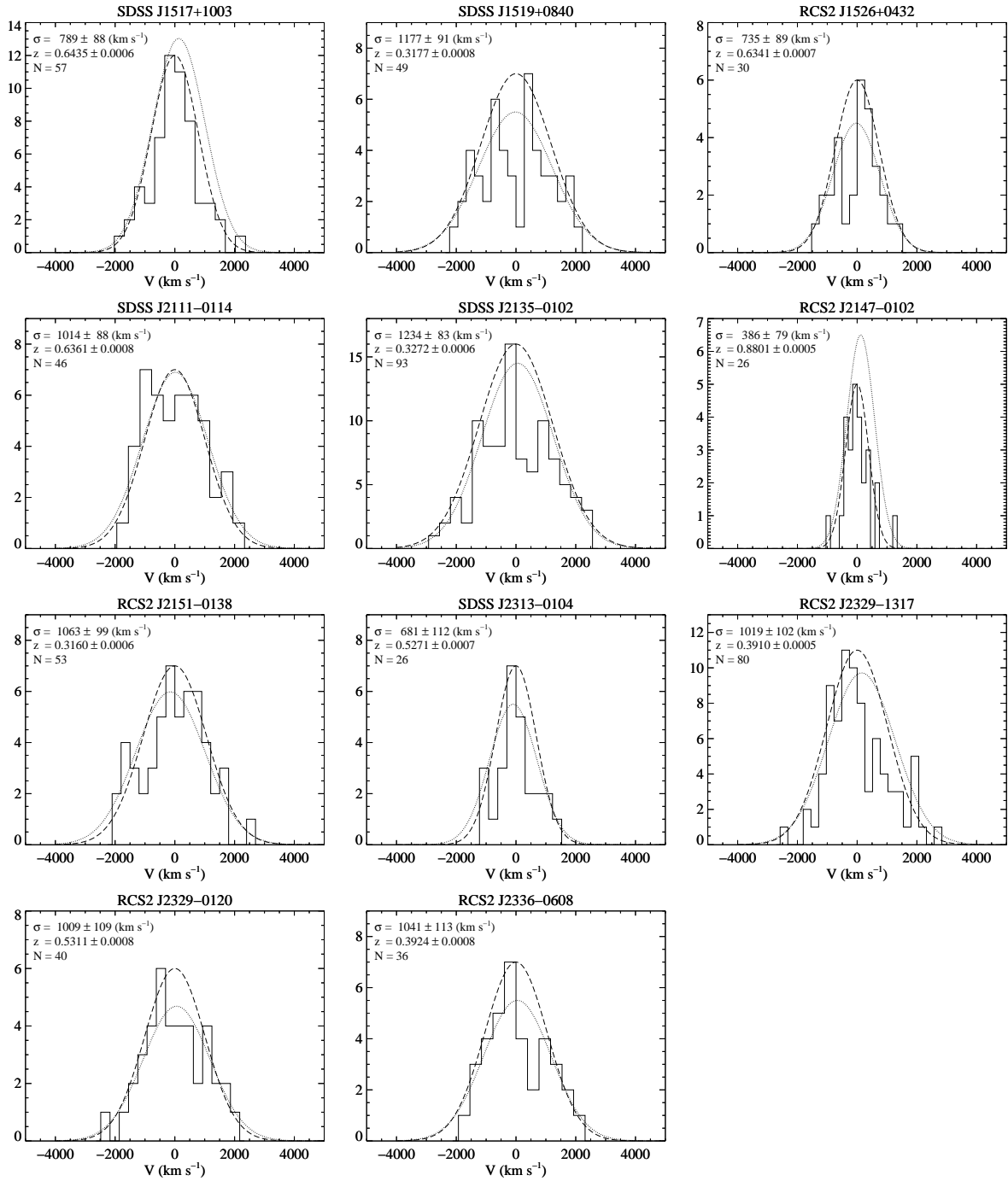


Figure 9. Velocity histograms for 11 out of 23 of our clusters with $N_{\text{mem}} \gtrsim 20$ showing a uni-modal distribution. The histograms are displayed in the same fashion as in Figure 8. Also, note that the y-axes differ between plots.

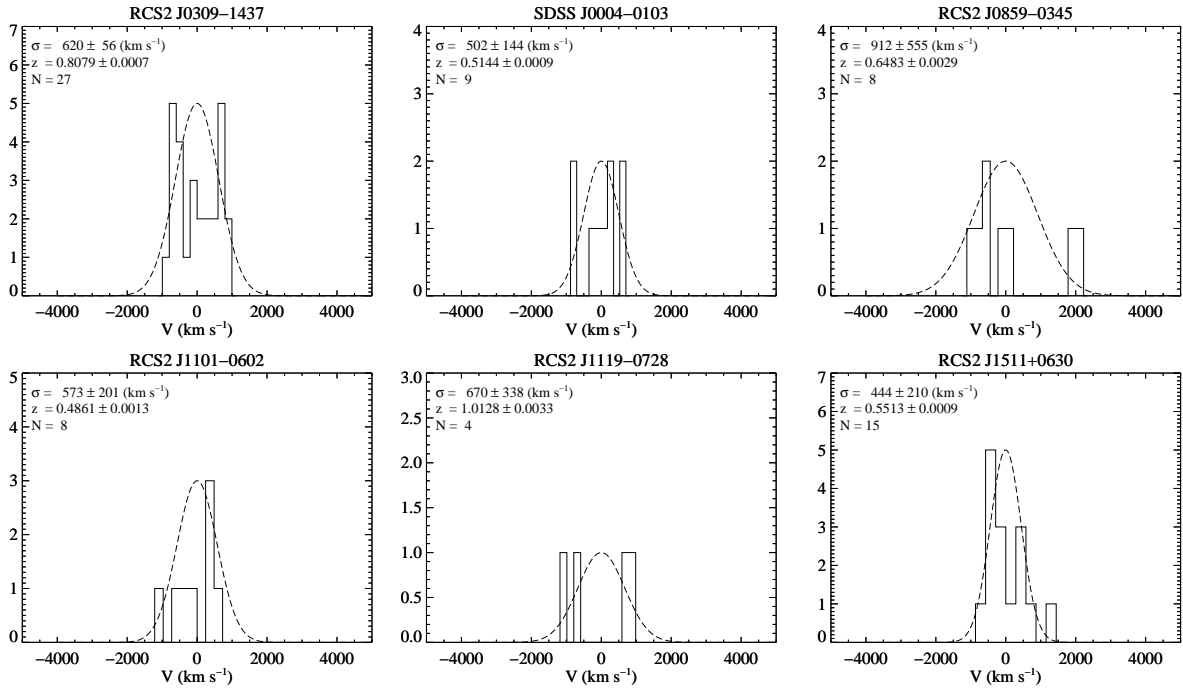


Figure 10. The upper left panel shows the velocity histogram of RCS2 J0309-1437, which is the only system in our sample (with $N_{\text{mem}} \gtrsim 20$) where the KS test suggests that its velocity distribution is not consistent with a uni-modal distribution. The other panels show the velocity histograms for five clusters with $N_{\text{mem}} \lesssim 20$, where the analysis of their velocity data is not possible due to the few number of spectroscopically confirmed cluster members. The histograms are displayed in the same fashion as in Figure 8. Dashed lines correspond to Gaussian distributions with the mean and variance equal to the first guess of the mean velocity and velocity dispersion squared of each cluster. Also, note that the y-axes differ between plots.

B. STRONG LENSING GALAXY CLUSTERS

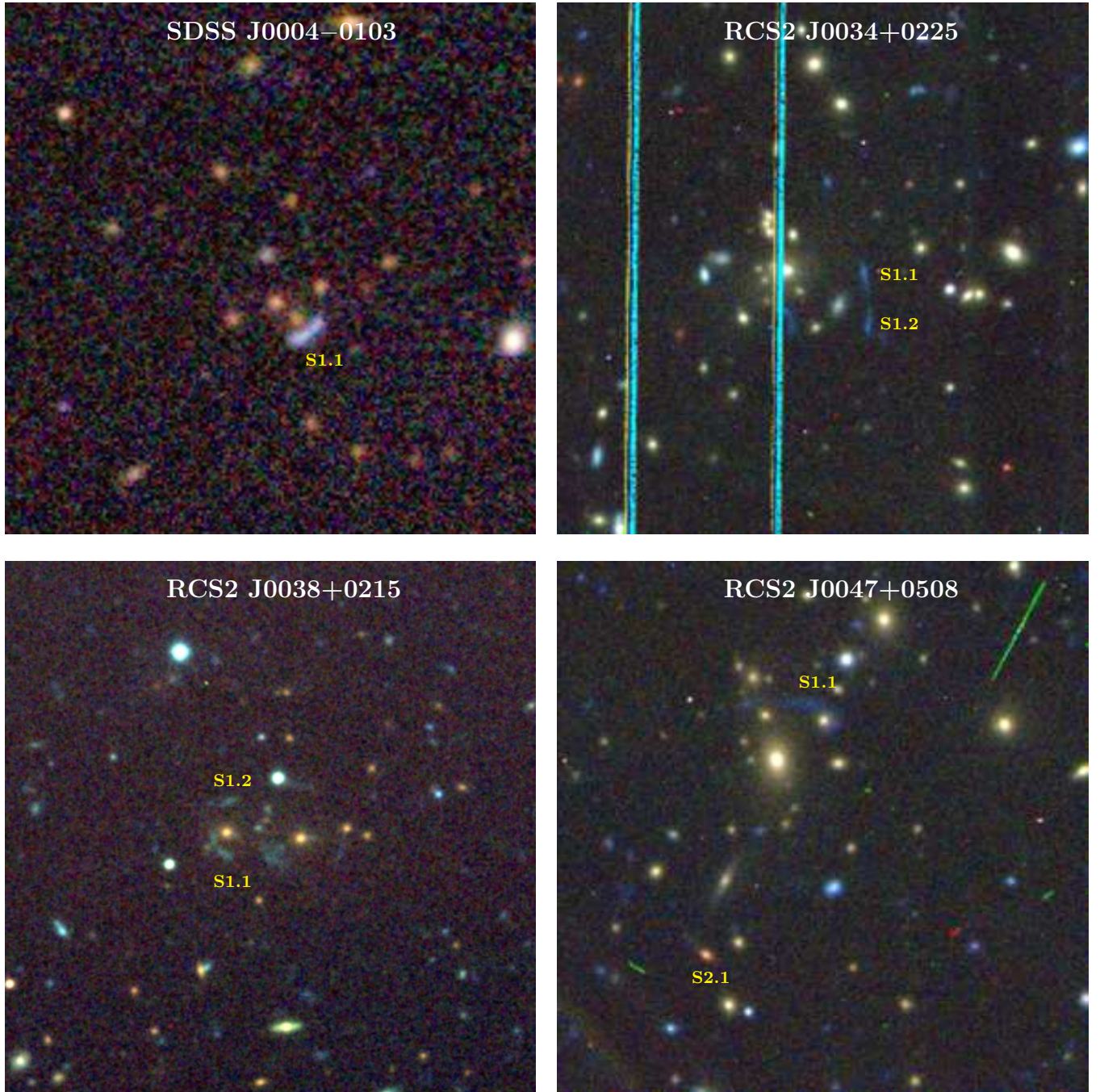


Figure 11. From the top-left to bottom-right panels we show the SL-selected galaxy clusters SDSS J0004-0103, RCS2 J0034+0225, RCS2 J0038+0215, and RCS2 J0047+0508. Lensed galaxies are labeled with markers that match the labels in Table 2, where their spectroscopic redshifts are shown. Objects labeled with the same identifier but different decimal numbers (S1.1, S1.2, etc) have the same redshifts within the errors, and we therefore assume that they correspond to multiple images of the same background source. Color composite images are made from *grz* imaging obtained from the RCS-2 survey with CFHT/MegaCam. All images cover a field of view of $75'' \times 75''$.

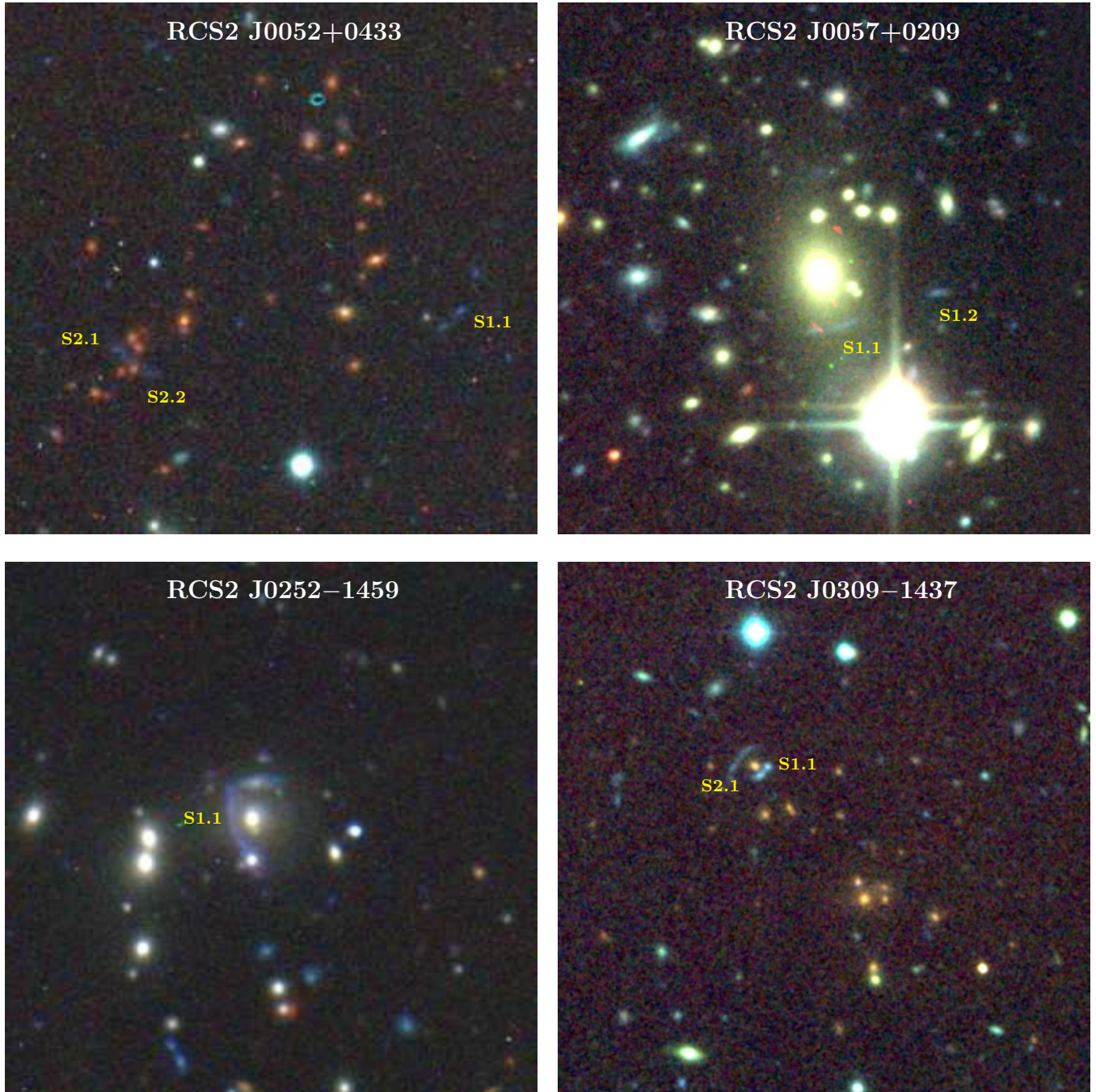


Figure 12. From the top-left to bottom-right panels we show the SL-selected galaxy clusters RCS2 J0052+0433, RCS2 J0057+0209, RCS2 J0252-1459, and RCS2 J0309-1437. Lensed galaxies are labeled in the same manner as in Figure 11. All images cover a field of view of $75'' \times 75''$.

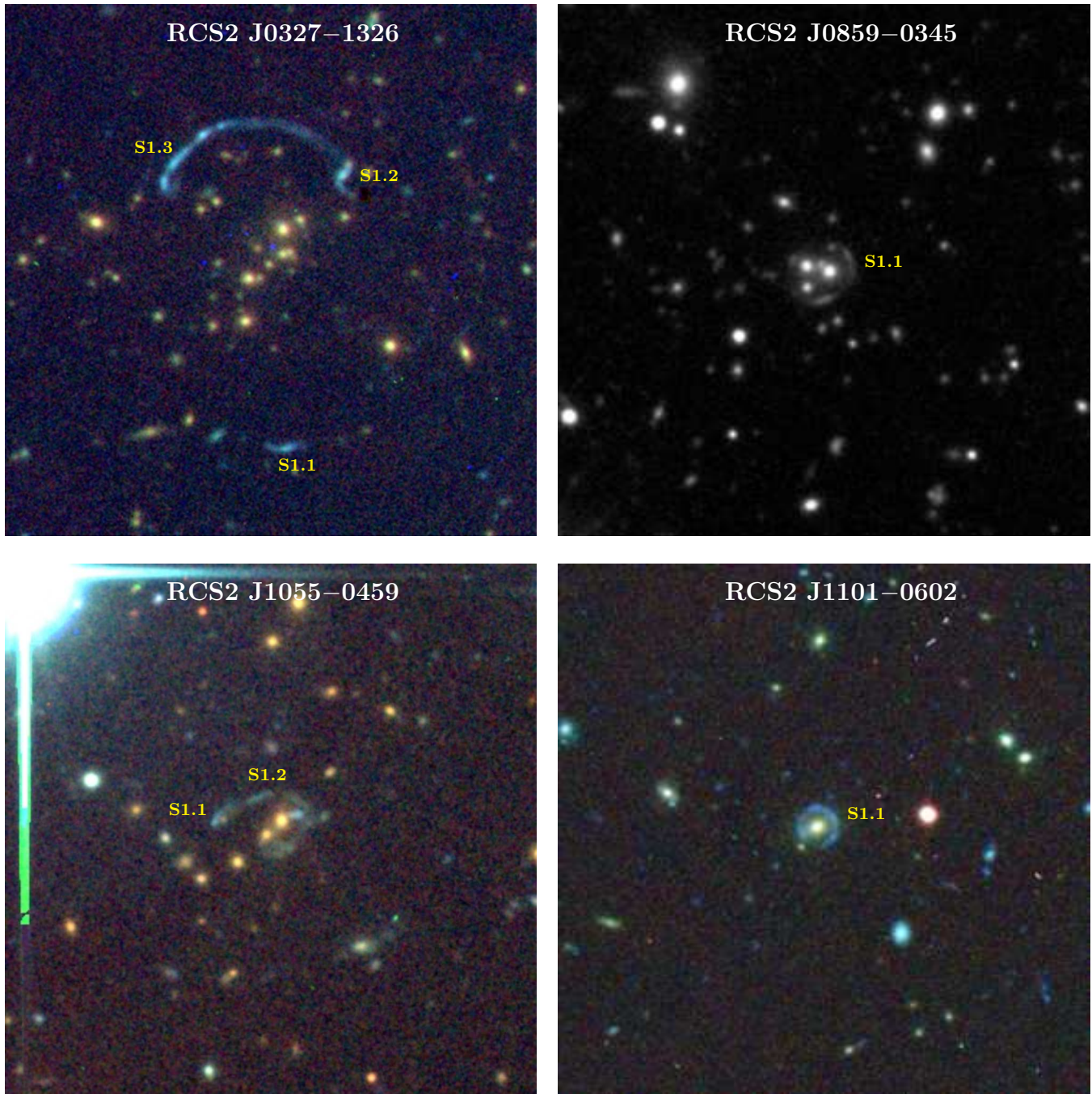


Figure 13. From the top-left to bottom-right panels we show the SL-selected galaxy clusters RCS2 J0327-1326, RCS2 J0859-0345, RCS2 J1055-0459, and RCS2 J1101-0602. Lensed galaxies are labeled in the same manner as in Figure 11. All images cover a field of view of $75'' \times 75''$.

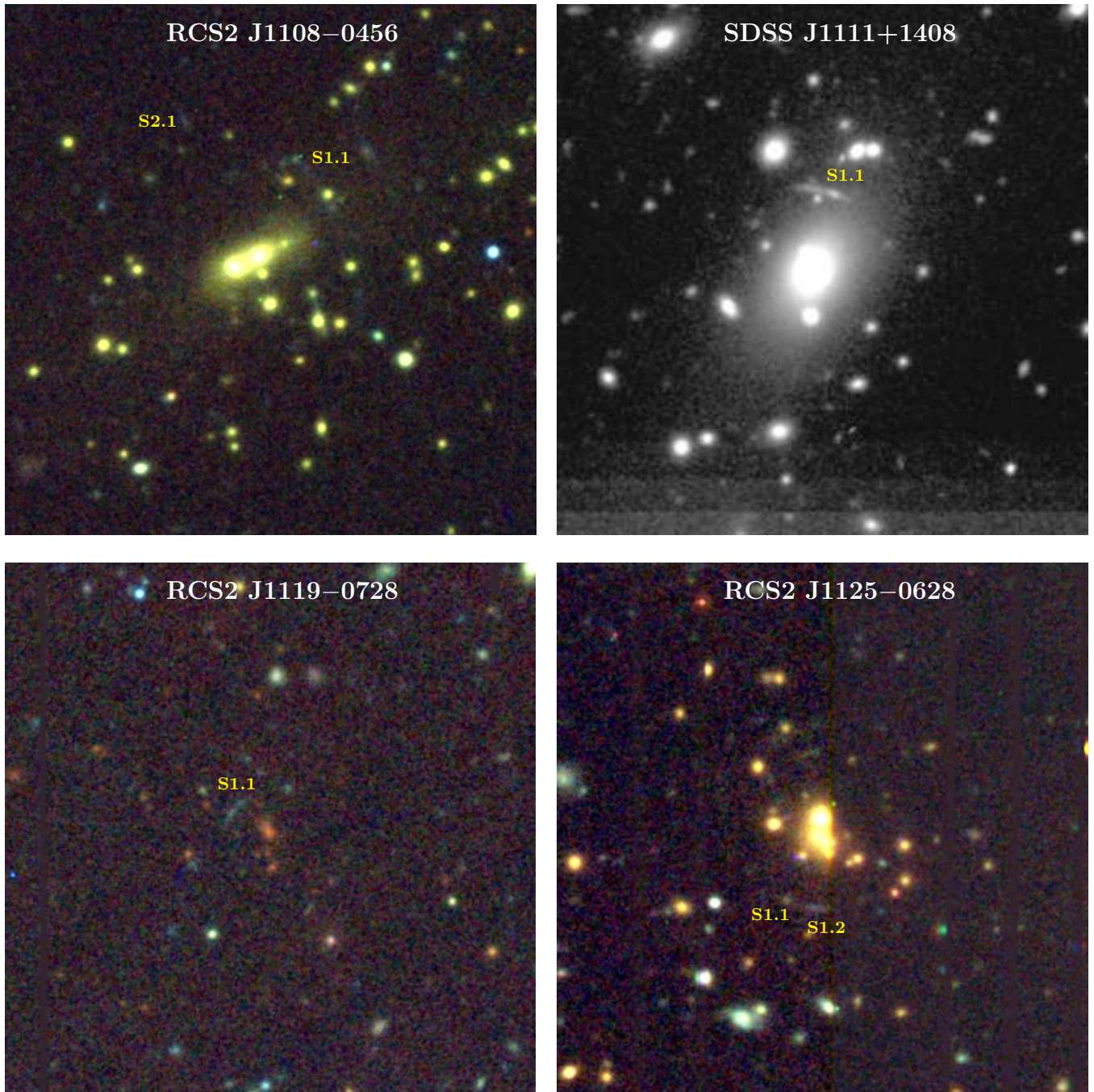


Figure 14. From the top-left to bottom-right panels we show the SL-selected galaxy clusters RCS2 J1108-0456, SDSS J1111+1408, RCS2 J1119-0728, and RCS2 J1125-0628. Lensed galaxies are labeled in the same manner as in Figure 11. All images cover a field of view of $75'' \times 75''$.

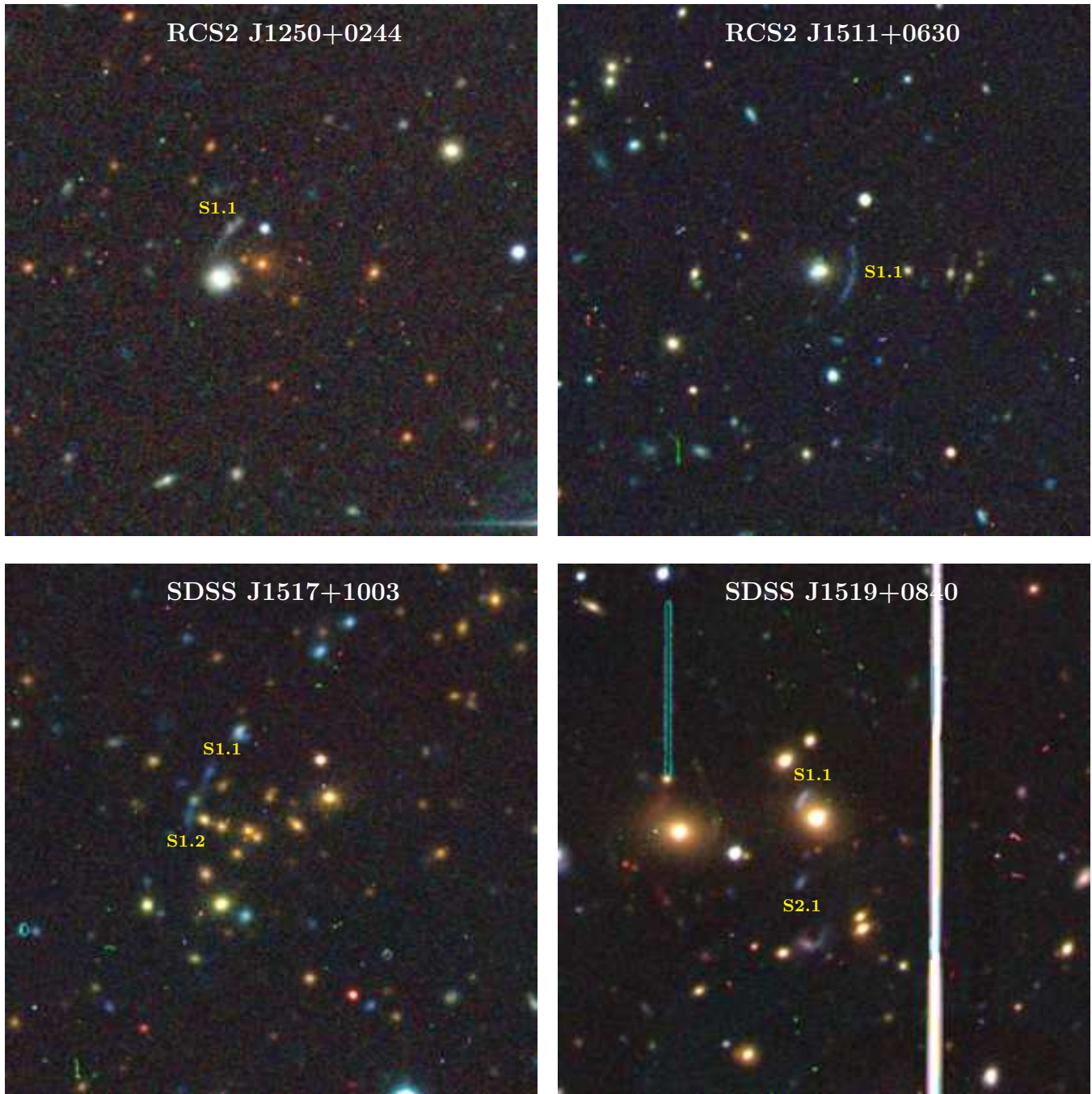


Figure 15. From the top-left to bottom-right panels we show the SL-selected galaxy clusters RCS2 J1250+0244, RCS2 J1511+0630, SDSS J1517+1003, and SDSS J1519+0840. Lensed galaxies are labeled in the same manner as in Figure 11. All images cover a field of view of $75'' \times 75''$.

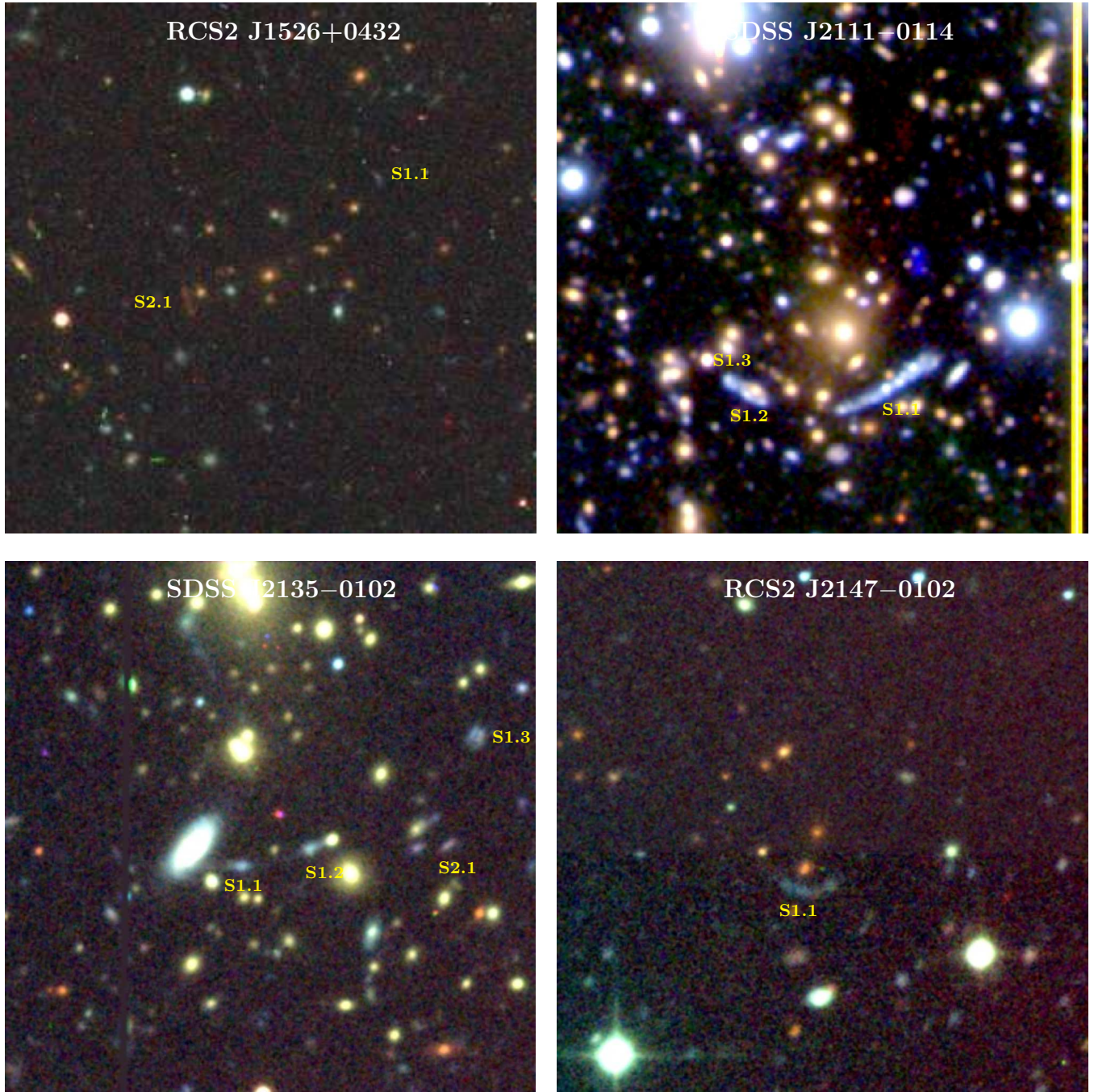


Figure 16. From the top-left to bottom-right panels we show the SL-selected galaxy clusters RCS2 J1526+0432, SDSS J2111-0114, SDSS J2135-0102, and RCS2 J2147-0102. Lensed galaxies are labeled in the same manner as in Figure 11. All images cover a field of view of $75'' \times 75''$. Galaxy cluster SDSS J2111-0114 is previously described in Bayliss et al. (2011b); its color composite image is made from *gri* imaging obtained with Subaru/SuprimeCam (Oguri et al. 2009).

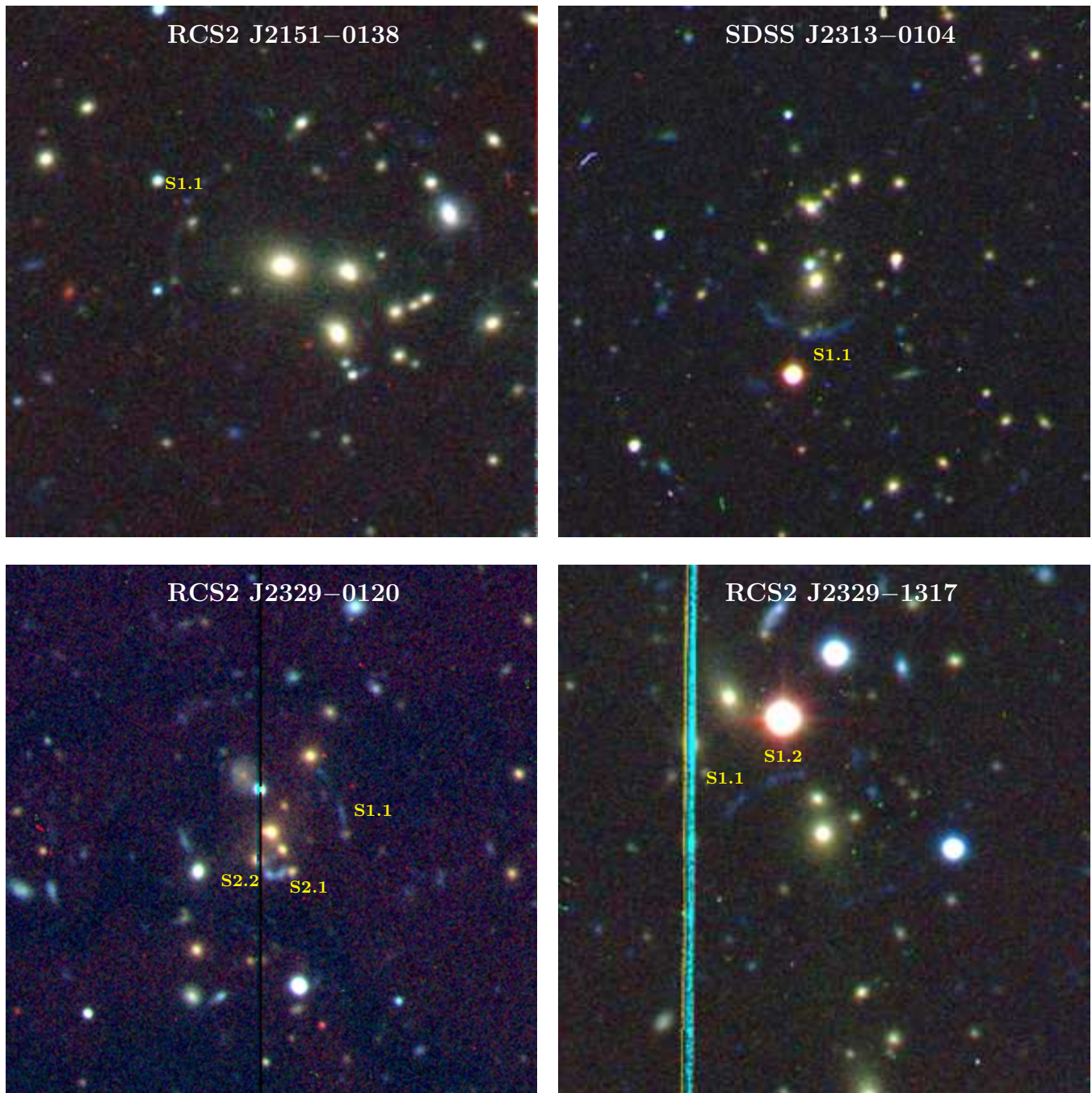


Figure 17. From the top-left to bottom-right panels we show the SL-selected galaxy clusters RCS2 J2151-0138, SDSS J2313-0104, RCS2 J2329-0120, and RCS2 J2329-1317. Lensed galaxies are labeled in the same manner as in Figure 11. All images cover a field of view of $75'' \times 75''$.

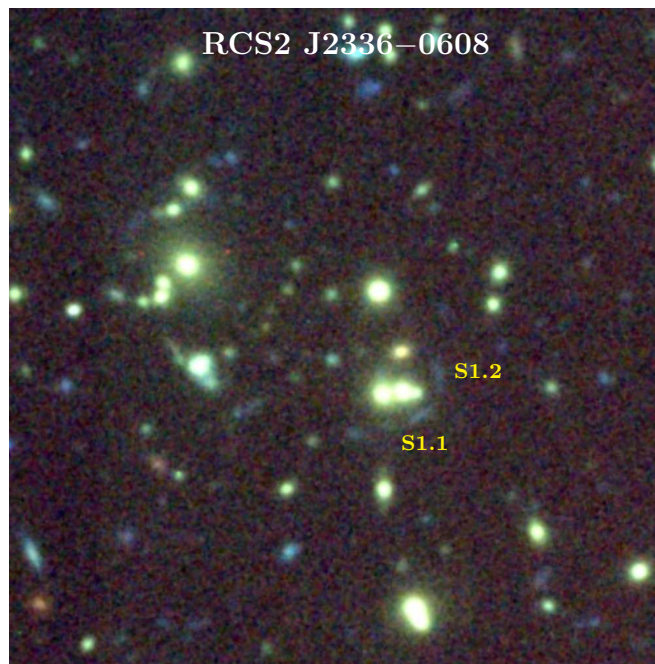


Figure 18. The SL-selected galaxy cluster RCS2 J2336–0608 is shown. Lensed galaxies are labeled in the same manner as in Figure 11. As in previous panels, the image covers a field of view of $75'' \times 75''$.